

Contents lists available at ScienceDirect

Petroleum Science

journal homepage: www.keaipublishing.com/en/journals/petroleum-science



Geological parameters and gas mixture composition on enhanced coalbed methane recovery: A THM modeling approach



Lei Yang ^{a, b}, Chao-Jun Fan ^{a, b, *}, Ming-Kun Luo ^{a, c}, Hai-Ou Wen ^{a, b}, Hao Sun ^{a, b}, Li-Jun Zhou ^a, Zhi-Heng Cheng ^{d, **}, Ze-Peng Zhang ^a

- ^a College of Mining, Liaoning Technical University, Fuxin, 123000, Liaoning, China
- ^b Ordos Institute, Liaoning Technical University, Ordos, 017004, Inner Mongolia, China
- ^c Energy Business Department, Shanxi Lu'an Chemical Group, Changzhi, 046200, Shanxi, China
- d School of Mine Safety, North China Institute of Science and Technology, Sanhe, 065201, Hebei, China

ARTICLE INFO

Article history: Received 26 November 2024 Received in revised form 6 February 2025 Accepted 8 February 2025 Available online 13 February 2025

Edited by Yan-Hua Sun

Keywords: GM-ECBM recovery THM coupled model Injection optimization Sensitivity analysis Permeability evolution

ABSTRACT

The utilization of coalbed methane (CBM) cannot only alleviate the energy crisis, but also reduce greenhouse gas emissions. Gas injection is an effective method to enhance CBM recovery. Compared to single-gas injection, the injection of CO₂/N₂ mixtures can balance the sharp decline in permeability caused by pure CO₂ and the premature breakthrough by pure N₂. In this study, a more comprehensive thermo-hydro-mechanical (THM) coupled mathematical model was developed, incorporating processes such as ternary gas non-isothermal adsorption, gas dissolution in water, gas-water two-phase flow, energy exchange, and coal deformation. After experimental validation, the model was applied to simulate the entire process of gas mixtures for enhanced CBM recovery (GM-ECBM). Results indicate that the permeability near the production well (PW) initially decreases due to increased effective stress, then increases as a result of CH4 desorption. Near the injection well (IW), the permeability first increases due to reduced effective stress and later stabilizes under the combined effects of effective stress and CO₂/N₂ adsorption. The initial CH₄ pressure and coal seam permeability have the most significant impact on CH₄ production, while the coal seam permeability and temperature significantly affect CO₂/N₂ injection. As the coal seam permeability increases, the optimal CO₂/N₂ ratio also increases accordingly. These findings provide important theoretical guidance for improving GM-ECBM efficiency in coal seams with varying permeabilities.

© 2025 The Authors. Publishing services by Elsevier B.V. on behalf of KeAi Communications Co. Ltd. This is an open access article under the CC BY license (http://creativecommons.org/licenses/by/4.0/).

1. Introduction

Coalbed methane (CBM), as a significant unconventional energy source due to its high energy and low pollutant, has great potential in alleviating the energy crisis (Du et al., 2023; Fang et al., 2023). However, CBM is also a major contributor to coal mine gas incidents, the greenhouse effect is 25 times greater than that of CO₂ posing a serious environmental threat (Li S. et al., 2023; Mukherjee and Misra, 2018; Pan et al., 2020). Additionally, the low recovery ratio commonly observed in CBM production seriously hinders its commercialization and scale development (Nie et al., 2023; Zhang C.L. et al., 2023).

E-mail addresses: chaojunfan@139.com (C.-J. Fan), chengzhiheng21@vip.qq.com (Z.-H. Cheng).

Although traditional hydraulic fracturing is effective in enhancing CBM recovery to some extent, its wide application is limited by high cost and potential environmental impacts (Fan et al., 2023a; Sun et al., 2023). In contrast, the use of gases such as CO₂, N₂, or their mixtures CO₂/N₂ enhanced CBM recovery (G-ECBM), has attracted significant interest due to its lower cost and environmental friendliness (Fujioka et al., 2010; Sun et al., 2016; Vishal et al., 2015; Zhou et al., 2022). G-ECBM increases pressure within the coalbed, accelerates CH₄ flow, and reduces CH₄ effective partial pressure, thereby promoting desorption of CH₄ (Fang et al., 2024; Ma et al., 2022; Shukla et al., 2010). This method not only effectively addresses the low recovery rates associated with declining reservoir pressure in late-stage of regular production, but also provides sustained momentum and stable migration pathways for fluid movement within the coalbed (Sun et al., 2018; Zarrouk and Moore, 2009). Moreover, G-ECBM offers the added environmental benefit by geological sequestration of greenhouse gases (Li Z.W. et al., 2023). Specifically, the gas mixtures (CO₂/N₂) effectively

^{*} Corresponding author.

^{**} Corresponding author.

prevent the rapid decrease in permeability around injection well (IW) caused by pure CO_2 injection, and avoids premature breakthrough by pure N_2 injection, thereby achieving efficient and stable CBM recovery (Fan et al., 2024).

In the GM-ECBM process, the injection gases enter the coalbed fractures through the IW, forming a two-phase flow with CH₄ and water within the fractures, exchanging mass transfer with the coal matrix, and diffuses into the matrix pores to displace adsorbed CH₄ (Asif et al., 2024; Zhang et al., 2023). The desorbed CH₄ then diffuses into the fractures and is driven by injected gas to the production well (PW) (Liu et al., 2024; Mwakipunda et al., 2023). This process involves competitive adsorption, diffusion, and seepage among CH₄, CO₂, and N₂. This dynamic evolution represents a complex interaction among coal, gas, and water (Liu X.D. et al., 2023a, 2023b). Research on GM-ECBM primarily focuses on laboratory experiments, field tests, and numerical simulations. Numerical simulation has been widely used for its advantages of low cost, fast results and repeatability. However, its accuracy largely depends on the quality of the mathematical model (Fan et al., 2024; Fang et al., 2024; Fujioka et al., 2008; Zhao et al., 2019).

The GM-ECBM mathematical model involves complex multiphysics coupling. Gas flow induces changes in pore pressure, affecting effective stress in the matrix (Fan et al., 2019a; Tupsakhare and Castaldi, 2019). Adsorption processes cause matrix swelling or shrinkage, altering porosity (Fan et al., 2021, 2023a; Sayyafzadeh et al., 2015). Gas adsorption/desorption and seepage together influence the temperature field (Masoudian, 2016; Xu et al., 2023). Conversely, increasing temperature accelerates gas desorption and flow, and changes gas density (Fan et al., 2020; Huo et al., 2019; Lin et al., 2018; Ren and Wang, 2015). The coal deformation energy alters the temperature field distribution, while thermal stress induced by temperature changes modifies the coal stress state (Ma et al., 2017; Shen et al., 2022; Wei et al., 2022). These factors collectively influence gas transport during GM-ECBM (Ma et al., 2023). Although these studies have established a solid theoretical foundation G-ECBM recovery, they have not fully addressed several key factors, as detailed in Table 1. Therefore, developing a fully coupled model that incorporates a more comprehensive range of interactions holds significant practical value for GM-ECBM recovery.

In addition, this technology is influenced by both geological parameters and injection CO_2/N_2 ratio. In this paper, an improved THM coupled mathematical model is established and applied to GM-ECBM simulations. By analyzing the influence of key geological parameters on GM-ECBM and the optimal injection ratio of CO_2/N_2 under different permeability conditions. The aim is to provide new insights and methods for the optimization of GM-ECBM technology, promoting its widespread application and maximizing its benefits.

2. THM model for GM-ECBM recovery

The schematic of the GM-ECBM process is shown in Fig. 1(a). To simplify the GM-ECBM process, we make the following assumptions before establishing the THM coupling model:

- (1) The coal seam is homogeneous and isotropic, as a linear elastic material. The coal mass consists of a dual-porosity medium formed by the matrix, matrix pores, and fractures.
- (2) CH₄, CO₂, and N₂ are predominantly adsorbed onto the inner surfaces of matrix pores, a portion of gases exists as the free phase within the pores and fractures (Fang et al., 2024). A small amount of gas dissolved in the water within the fracture system, water vapor is present in the fractures (Fan et al., 2021).
- (3) Free gases follow the ideal gas law (Li Z.W. et al., 2023).
- (4) Gas diffusion and adsorption in fractures are neglected, and fluid seepage in the matrix is considered negligible.
- (5) The transport of gas from matrix pores to the fracture system involves two processes (Fig. 1(b)): desorption and diffusion (Fan et al., 2023b). Adsorption and desorption are reversible processes that follow the extended Langmuir law (Huo et al., 2019). The desorbed free CH₄ transports from the matrix pore wall to fracture governed by a concentration gradient and following Fick's law (Fan et al., 2020). The CH₄ in the fractures flows into the PW according to Darcy's law. The transportation process of CO₂/N₂ is opposite to that of CH₄ (Shen et al., 2022).
- (6) The effective stress exerted by gas on the coal framework is calculated using the modified Terzaghi effective stress principle (Zhou et al., 2022).
- (7) The effective stress and gas adsorption-desorption alters the size of the pores and fractures (Liu Z.D. et al., 2023) (Fig. 1(c)).
- (8) It is assumed that the temperature within the coalbed is continuous, and at any given point, the temperature of the water, gas, and coal mass are equal.

2.1. Porosity and permeability model

The matrix porosity is the ratio of the coal matrix volume to the matrix pore volume, and the change in matrix porosity is primarily influenced by matrix strain. The evolution equation of matrix porosity can be described as (Fan et al., 2024):

$$\varphi_{\rm m} = \varphi_{\rm m0} \exp\left(\frac{1 - \varphi_{\rm m0}}{\varphi_{\rm m0}} \Delta \varepsilon_{\rm m}\right) \tag{1}$$

Table 1Comparison of different coupling models.

Model source	Key factors									
	Double porosity	Two phase flow	Coal deformation	Heat transfer	Ternary (binary) gases non-isothermal adsorption	Dissolved gas	Water vapor			
Fan et al. (2020)	<u> </u>		<u> </u>	1	Ternary gas, isothermal					
Fang et al. (2024) Li Z.W. et al. (2023)	✓		✓	✓	Binary gas, non-isothermal					
Lin et al. (2018)	✓		✓		Binary gas, isothermal					
Liu Z.D. et al. (2023)	✓		✓	1	Binary gas, non-isothermal					
Liu X.D. et al. (2023a)	✓	✓	✓	✓	Binary gas, non-isothermal	✓				
Ma et al. (2017)	✓	✓			Binary gas, isothermal					
Sayyafzadeh et al. (2015)		✓	✓		Ternary gas, isothermal					
Sun et al. (2016)	✓	✓	✓		Binary gas, isothermal					
Vishal et al. (2015)	✓	✓			Binary gas, isothermal					

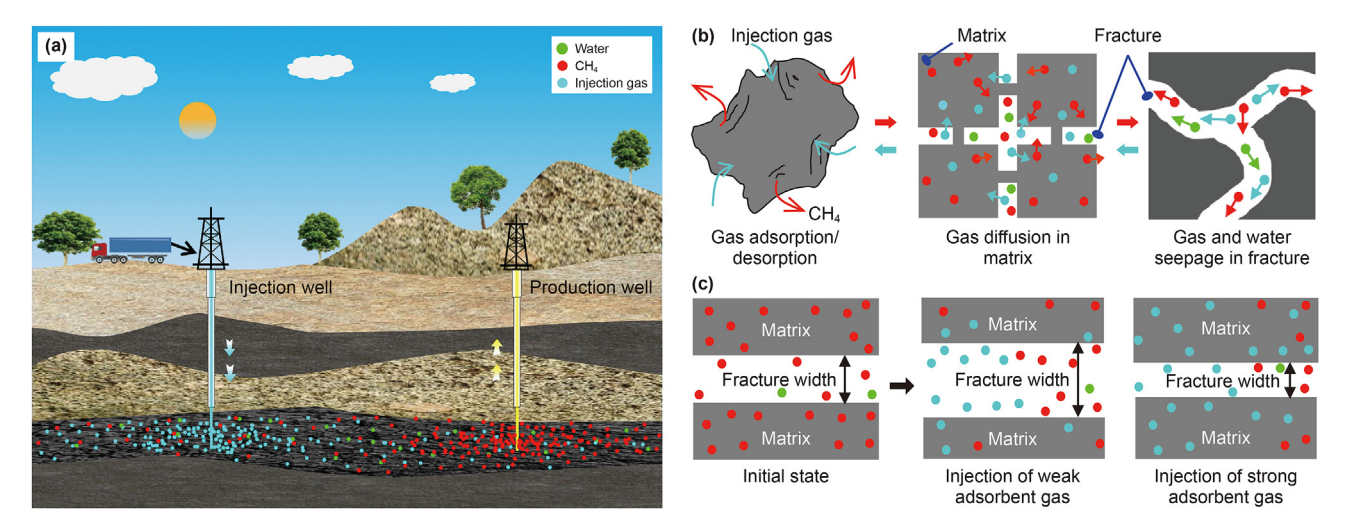


Fig. 1. GM-ECBM recovery diagram. (a) Schematic of GM-ECBM process; (b) Gas migration process; (c) Changes in fractures.

where φ_{m0} is the initial matrix porosity; $\Delta \varepsilon_m$ is the total strain of coal matrix, which is primarily determined by effective stress, temperature, and gas adsorption/desorption.

$$\Delta \varepsilon_{\rm m} = \Delta \varepsilon_{\rm m}^{\rm E} + \Delta \varepsilon_{\rm m}^{\rm T} + \Delta \varepsilon_{\rm m}^{\rm S} \tag{2}$$

The mechanical strain caused by changes in effective stress is related to the matrix shear modulus $K_{\rm m}$ as follows (Fan et al., 2019a):

$$\begin{cases} \Delta \varepsilon_{\rm m}^{\rm E} = -\frac{\Delta \sigma_{\rm em}}{K_{\rm m}} \\ \Delta \sigma_{\rm em} = \Delta \overline{\sigma} - \alpha_{\rm m} \Delta p_{\rm m} - \alpha_{\rm f} \Delta p_{\rm f} \end{cases}$$
 (3)

where $\Delta\sigma_{\rm em}$ is the effective stress of the matrix, MPa; $K_{\rm m}$ is the matrix shear modulus, MPa; $\overline{\sigma}$ is the average effective stress, MPa; $\alpha_{\rm m}$ is the matrix pore Biot coefficient; $p_{\rm m}=p_{\rm m1}+p_{\rm m2}+p_{\rm m3}$ is the matrix gas pressure, MPa, where 1, 2 and 3 represent CH₄, CO₂, and N₂, respectively; $\alpha_{\rm f}$ is the Biot coefficient of fracture; $p_{\rm f}=p_{\rm fw} \cdot s_{\rm w}+p_{\rm fg} \cdot s_{\rm g}$ is the fracture fluid pressure, MPa; $p_{\rm fw}=p_{\rm fg1}+p_{\rm fg2}+p_{\rm fg3}-p_{\rm cgw}$ is the pressure of water in the fracture, MPa; $s_{\rm w}$ is the water saturation; $p_{\rm cgw}$ is the capillary pressure, MPa; $p_{\rm fg}=p_{\rm fg1}+p_{\rm fg2}+p_{\rm fg3}$ is the gas pressure in the fracture, MPa; $s_{\rm g}$ is the gas saturation; $s_{\rm g}+s_{\rm w}=1$; subscript 0 represents the initial value of the variable.

The matrix strain resulting from temperature variations is represented by the following:

$$\Delta \varepsilon_{\rm m}^{\rm T} = -\alpha_{\rm T} \Delta T \tag{4}$$

where α_T is the thermal expansion coefficient of coal skeleton, 1/K. Matrix strain induced by gas competitive adsorption is represented by the following (Fan et al., 2019a; Liu X.D. et al., 2023a, 2023b; Liu et al., 2019; Meng et al., 2019):

$$\begin{cases} \Delta \varepsilon_{\rm m}^{\rm S} = \sum_{i=1}^{3} \left(\varepsilon_{\rm mi}^{\rm S} - \varepsilon_{\rm mi0}^{\rm S} \right) \\ \varepsilon_{\rm mi}^{\rm S} = \varepsilon_{\rm Li} V_{\rm sgi} = \varepsilon_{\rm Li} \frac{V_{\rm Li} p_{\rm mgi} \exp(-d_2 (T - T_{\rm t})/(1 + d_1 p_{\rm m}))}{P_{\rm Li} + P_{\rm Li} \left(b_{\rm L1} p_{\rm mg1} + b_{\rm L2} p_{\rm mg2} + b_{\rm L3} p_{\rm mg3} \right)} \end{cases}$$

$$(5)$$

where ε_{Li} is the strain coefficient of the coal adsorbed gas; V_{sgi} is the adsorption amount of gas in the matrix, m³/kg; p_{mgi} is the pressure

of gas component i in the matrix, MPa; T is the temperature of coal reservoir, K; T_t is the laboratory adsorption reference temperature, K; V_{Li} is the Langmuir volume constant of gas, m^3/kg ; d_1 is the pressure coefficient of non-isothermal adsorption, 1/MPa; d_2 is the temperature coefficient of non-isothermal adsorption, 1/K; P_{Li} is the Langmuir pressure constant of gas, MPa.

The fracture strain is caused by matrix/fracture effective stress, gas adsorption/desorption, and temperature, as shown in Fig. 2. The volume strain of the representative element volume (REV) by the following (Fang et al., 2024; Li Z.W. et al., 2023):

$$\Delta \varepsilon_{\rm v} = \frac{a^3}{s^3 K_{\rm m}} \Delta \sigma_{\rm em} + \frac{s^3 - a^3}{s^3 K_{\rm f}} \Delta \sigma_{\rm ef} - \frac{a^3}{s^3} \Delta \varepsilon_{\rm m}^{\rm S} - \frac{a^3}{s^3} \alpha_{\rm T} \Delta T \tag{6}$$

where a is the matrix width, m; s is the width of the REV, m; K_f is equivalent fracture stiffness, GPa.

Assuming r_{as} represents the ratio of coal matrix width to REV width, the change of the fracture effective stress can be derived from Eq. (6) as shown (Zhou et al., 2022):

$$\Delta\sigma_{\rm ef} = \frac{K_{\rm m}K_{\rm f}}{K_{\rm f}r_{\rm as}^3 + K_{\rm m} - K_{\rm m}r_{\rm as}^3} \left(\frac{r_{\rm as}^3}{K_{\rm m}}\alpha_{\rm m}\Delta p_{\rm m} + r_{\rm as}^3\Delta\varepsilon_{\rm m}^{\rm S} + r_{\rm as}^3\alpha_{\rm T}\Delta T + \Delta\varepsilon_{\rm v}\right)$$

$$(7)$$

The fracture porosity is defined as the sum of the initial porosity and its subsequent increase (Zhang Q. et al., 2023):

$$\begin{cases} \varphi_{\rm f} = \varphi_{\rm f0} + \varphi_{\rm f0} \frac{\Delta b}{b} \\ \Delta b = \frac{b}{3K_{\rm f}} \Delta \sigma_{\rm ef} \end{cases}$$
 (8)

where φ_{f0} is the initial fracture porosity.

Substituting Eq. (7) into Eq. (8), the evolution equation for fracture porosity as (Fan et al., 2024; Liu Z.D. et al., 2023)

$$\varphi_{f} = \varphi_{f0} + \frac{\varphi_{f0}K_{m}}{3\left(K_{f}r_{as}^{3} + K_{m} - K_{m}r_{as}^{3}\right)} \left(\frac{r_{as}^{3}}{K_{m}}\alpha_{m}\Delta p_{m} + r_{as}^{3}\Delta\varepsilon_{m}^{S}\right) + r_{as}^{3}\alpha_{T}\Delta T + \Delta\varepsilon_{v}$$

$$(9)$$

The relationship between coalbed permeability and fracture porosity follows the cubic law:

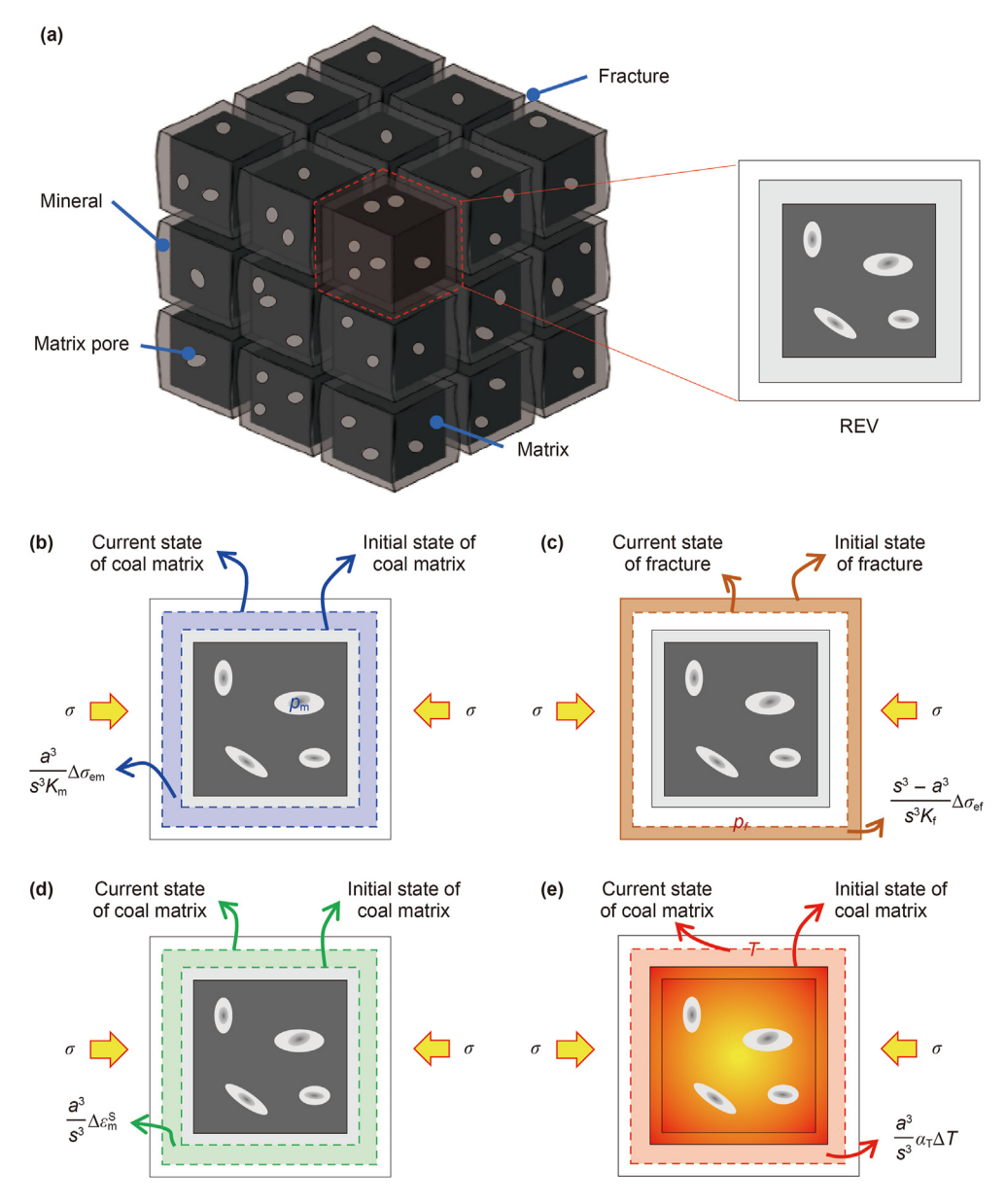


Fig. 2. Schematic diagram of the RVE deformation. (a) Physical model of dual-porosity medium; (b) Matrix effective stress effect; (c) Fracture effective stress effect; (d) Gas adsorption/desorption effect; (e) Thermal effect.

$$k = k_0 \left(1 + \frac{K_{\rm m}}{3 \left(K_{\rm f} r_{\rm as}^3 + K_{\rm m} - K_{\rm m} r_{\rm as}^3 \right)} \left(\frac{r_{\rm as}^3}{K_{\rm m}} \alpha_{\rm m} \Delta p_{\rm m} + r_{\rm as}^3 \Delta \varepsilon_{\rm m}^5 + r_{\rm as}^3 \alpha_{\rm T} \Delta T + \Delta \varepsilon_{\rm v} \right) \right)^3$$
(10)

where k_0 is the initial permeability of coalbed, mD.

2.2. Governing equation of fluid transport

2.2.1. Gas transport equation in matrix

The total gas mass in the matrix is composed of both adsorbed

gas and free gas. Free gas follows the ideal gas law, while the non-isothermal competitive adsorption of multicomponent gases is characterized by the extended Langmuir equation. The gas mass per unit volume of the matrix is (Fan et al., 2019a)

$$m_{\text{matrix}i} = \varphi_{\text{m}} \frac{M_{\text{gi}}}{RT} p_{\text{mgi}} + V_{\text{sgi}} \rho_{\text{c}} \rho_{\text{gsi}}$$
(11)

where $M_{\rm gi}$ is the gas molar mass, g/mol; R is the gas molar constant, J/(mol·K); $\rho_{\rm c}$ is the coal density, kg/m³; $\rho_{\rm gsi}$ is the gas density under standard conditions, kg/m³.

The variation in gas content per unit volume of matrix is

$$\frac{\partial m_{\text{matrix}i}}{\partial t} = F_{\text{matrix}i} \tag{12}$$

where $F_{\text{matrix}i}$ is the mass source of the gas in the matrix.

The exchange of ternary gases between the matrix and fractures is primarily governed by diffusion. The source term of gas mass within the matrix is (Fan et al., 2021, 2023b)

$$F_{\text{matrix}i} = -\frac{M_{\text{gi}}}{\tau_i RT} \left(p_{\text{mgi}} - p_{\text{fgi}} \right) \tag{13}$$

where p_{fgi} is the gas pressure in the fractures, MPa; τ_i is the desorption time of gas, d.

Substituting Eqs. (11) and (12) into Eq. (13), the gas diffusion governing equation in GM-ECBM process can be derived

$$\frac{\partial}{\partial t} \left\{ \varphi_{\rm m} \frac{M_{\rm gi}}{RT} p_{\rm mgi} + V_{\rm sgi} \rho_{\rm c} \rho_{\rm gsi} \right\} = -\frac{M_{\rm gi}}{\tau_{\rm i} RT} \left(p_{\rm mgi} - p_{\rm fgi} \right) \tag{14}$$

2.2.2. Fluid transport governing equation in fracture

The CH₄ desorption from the surface of the matrix pores provides a mass source for CH₄ within the fractures, while the injection gas functions as a mass sink for gas adsorption within the matrix. The fracture system contains multiple gas, water, dissolved gas and water vapor, its seepage process satisfies Darcy's law. Based on the principle of mass conservation, the transport equation of gas-water mixture within fractures is obtained (Liu X.D. et al., 2023a, 2023b)

obtained according to Henry's law and Kelvin Laplace's law (Fan et al., 2024):

$$\begin{cases} \rho_{\rm dgi} = H_{\rm gi} \rho_{\rm fgi} \\ \rho_{\rm v} = \rho_{\rm vs} h = \rho_{\rm vs} \exp \left(p_{\rm cgw} / \rho_{\rm w} R_{\rm v} T \right) \end{cases}$$
 (16)

where H_{gi} is the Henry coefficient of gas; ρ_{vs} is the density of saturated steam, kg/m³; h is relative humidity; R_v is the latent heat of steam, J/(K·kg).

The seepage velocity of both gas and water phase within fracture is (Sun et al., 2016)

$$\begin{cases} v_{gi} = -\frac{kk_{rg}}{\mu_{gi}} \left(1 + \frac{b_k}{p_{fgi}} \right) \nabla p_{fgi} \\ v_{W} = -\frac{kk_{rW}}{\mu_{W}} \nabla p_{fw} \end{cases}$$
(17)

where $k_{\rm rg}$ is the relative permeability of gas; $b_{\rm k}$ is Klinkenberg factor, MPa; $k_{\rm rw}$ is the relative permeability of water; $\mu_{\rm gi}$ is the dynamic viscosity of gas, MPa·s; $\mu_{\rm w}$ is the dynamic viscosity of water, MPa·s.

The relative permeability of gas and water is influenced by the saturation of the gas and water flow (Ren and Wang, 2015; Shen et al., 2022):

$$\begin{cases}
k_{rg} = k_{rg0} \left[1 - \left(\frac{s_{w} - s_{wr}}{1 - s_{wr} - s_{gr}} \right) \right]^{2} \left[1 - \left(\frac{s_{w} - s_{wr}}{1 - s_{wr}} \right)^{2} \right] \\
k_{rw} = k_{rw0} \left(\frac{s_{w} - s_{wr}}{1 - s_{wr}} \right)^{4}
\end{cases} (18)$$

where k_{rg0} is the endpoint relative permeability of the gas; k_{rw0} is the endpoint relative permeability of the water; s_{wr} is the saturation of bound water; s_{gr} is the residual gas saturation.

Substituting Eqs. (16)–(18) into Eq. (16), the transport equation

$$\begin{cases}
\frac{\partial \left(s_{g} \varphi_{f} \rho_{fgi} \right)}{\partial t} + \frac{\partial \left(s_{w} \varphi_{f} \rho_{dgi} \right)}{\partial t} = \frac{M_{gi}}{\tau_{i} RT} \left(p_{mgi} - p_{fgi} \right) + \nabla \cdot \left(\rho_{fgi} \nu_{gi} \right) + \nabla \cdot \left(\rho_{dgi} \nu_{w} \right) \\
\frac{\partial \left(s_{w} \varphi_{f} \rho_{w} \right)}{\partial t} + \frac{\partial \left(s_{w} \varphi_{f} \rho_{v} \right)}{\partial t} = \nabla \cdot \left(\rho_{w} \nu_{w} \right) + \nabla \cdot \left(\rho_{v} \sum_{i=1}^{3} \nu_{gi} \right)
\end{cases} \tag{15}$$

where ρ_{fgi} is the density of gas in the fracture, kg/m³; ρ_{w} is the density of water under standard conditions, kg/m³; ρ_{dgi} and ρ_{v} are the densities of dissolved gas and water vapor, kg/m³; which can be

of gas-water mixture in fractures can be derived

$$\begin{cases}
\frac{\partial \left(s_{g}\varphi_{f}\rho_{fgi}\right)}{\partial t} + \frac{\partial \left(s_{w}\varphi_{f}H_{gi}\rho_{fgi}\right)}{\partial t} = \frac{M_{gi}}{\tau_{i}RT}\left(p_{mgi} - p_{fgi}\right) + \nabla \cdot \left(\frac{M_{gi}\left(p_{fgi} + b_{k}\right)kk_{rg}}{RT\mu_{gi}}\nabla p_{fgi}\right) + \nabla \cdot \left(\frac{H_{gi}\rho_{fgi}kk_{rw}}{\mu_{w}}\nabla p_{fw}\right) \\
\frac{\partial \left(s_{w}\varphi_{f}\rho_{w}\right)}{\partial t} + \frac{\partial}{\partial t}\left(s_{g}\varphi_{f}\rho_{vs}\exp\left(\frac{p_{rgw}}{\rho_{w}R_{v}T}\right)\right) = \nabla \cdot \left(\frac{\rho_{w}kk_{rw}}{\mu_{w}}\nabla p_{fw}\right) + \nabla \cdot \left(\rho_{vs}\exp\left(\frac{p_{rgw}}{\rho_{w}R_{v}T}\right)\sum_{i=1}^{3}\frac{kk_{rg}}{\mu_{gi}}\left(1 + \frac{b_{k}}{p_{fgi}}\right)\nabla p_{fgi}\right)
\end{cases}$$
(19)

2.3. Temperature field governing equation

In the GM-ECBM process, different components within the coal mass, such as the coal matrix, multi-phase gases, water and water vapor interact, leading to complex energy exchange phenomena. The thermodynamic interactions and changes among these components play a significant role in the GM-ECBM recovery. Specifically, the energy exchange during this process involves several factors: the internal energy change induced by temperature variations, the strain energy resulting from the volume deformation of coal, isosteric heat induced by gas adsorption, and the heat convection and conduction between the solid phase and fluid phase. Assuming the system reaches thermal equilibrium, the energy exchange in the GM-ECBM process can be expressed as (Durucan et al., 2013; Fan et al., 2021; Rutqvist et al., 2002)

$$\frac{\partial}{\partial t} \left(\left(\rho C_{p} \right)_{s+f} T \right) + \eta_{s+f} \nabla T - \nabla \cdot \left(\lambda_{s+f} \nabla T \right) + K \alpha_{T} T \frac{\partial \varepsilon_{V}}{\partial t} \\
+ \sum_{i=1}^{3} q_{sti} \frac{\rho_{c} \rho_{gsi}}{M_{\sigma i}} \frac{\partial V_{sgi}}{\partial t} = 0$$
(20)

where $(\rho C_p)_{s+f}$ is the effective specific heat capacity of coal, J/ $(m^3 \cdot K)$; η_{s+f} is the effective convection coefficient of the fluid, J/ $(m^2 \cdot s)$; λ_{s+f} is the effective thermal conductivity of coal, W/($m \cdot K$); q_{sti} is the isosteric heat of gas adsorption, kJ/mol.

The effective specific heat capacity of coal is determined by the density and specific heat capacities of its internal components (Zhou et al., 2022):

$$\begin{split} \left(\rho C_{p}\right)_{s+f} &= \left(1 - \varphi_{f} - \varphi_{m}\right) \rho_{s} C_{s} \\ &+ \sum_{i=1}^{3} \left(s_{g} \varphi_{f} \rho_{fgi} + \varphi_{m} \rho_{mgi} + s_{w} \varphi_{f} \rho_{dgi}\right) C_{gi} + s_{w} \varphi_{f} \rho_{w} C_{w} + s_{g} \varphi_{f} \rho_{v} C_{v} \end{split} \tag{21}$$

where C_s , C_{gi} , C_w , C_v are the specific heat capacities of coal skeleton, gas, water and water vapor respectively, $J/(kg \cdot K)$.

The effective heat convection coefficient of the fluid mixture is related to the convective heat transfer between the gas and water in the fractures (Fan et al., 2024):

$$\eta_{s+f} = -\sum_{i=1}^{3} \left(\frac{\rho_{fgi} C_{gi} k k_{rg}}{\mu_{gi}} \left(1 + \frac{b_{k}}{p_{fgi}} \right) \nabla p_{fgi} + \frac{H_{gi} \rho_{fgi} C_{gi} k k_{rw}}{\mu_{w}} \nabla p_{fw} \right) \\
- \left(\rho_{v} \sum_{i=1}^{3} \frac{C_{w} k k_{rg}}{\mu_{gi}} \left(1 + \frac{b_{k}}{p_{fgi}} \right) \nabla p_{fgi} + \frac{\rho_{w} C_{w} k k_{rw}}{\mu_{w}} \nabla p_{fw} \right) \tag{22}$$

The effective thermal conductivity of the coal mass is a linear combination of the thermal conductivities of each component (Liu X.D. et al., 2023a):

$$\lambda_{s+f} = (1 - \varphi_f - \varphi_m)\lambda_s + \varphi_m\lambda_{mg} + \varphi_f s_g \lambda_{fg} + \varphi_f s_w \lambda_{fw}$$
 (23)

where λ_s , λ_{mg} , λ_{fg} , λ_{fw} are the thermal conductivity of coal skeleton, mixed gas in matrix, mixed gas and water in fracture, W/(m·K), respectively.

For the gas mixture, the thermal conduction coefficient is defined as follows (Fan et al., 2019a):

$$\lambda = \frac{1}{2} \left(\sum_{i=1}^{M} x_i \lambda_i + \left(\sum_{i=1}^{M} x_i / \lambda_i \right)^{-1} \right)$$
 (24)

where λ is the heat conduction coefficient of the gas mixture, W/

 $(m \cdot K)$; x_i is the mole fraction of the gas; λ_i is the thermal conductivity of the gas, $W/(m \cdot K)$; M is the number of components of a gas.

2.4. Governing equations for coal deformation

Based on the assumption that the coal mass is a linear elastic material, it will undergo elastic deformation under the influence of geostress and fluid pressure. The stress equilibrium equation in this process, also known as the Navier equation, can be expressed in tensor form (Dai et al., 2024; Wu et al., 2011; Yang et al., 2023):

$$\sigma_{ki,i} + F_k = 0 \tag{25}$$

where σ is the stress exerted on the coal, MPa; F is the body force, N; k and j denote the x, y, and z directions.

In the Cartesian coordinate system, the relationship between the strain components and displacement components satisfies the Cauchy equation, which can be expressed in tensor form (Liu Z.D. et al., 2023; Zhou et al., 2013):

$$\varepsilon_{kj} = \frac{1}{2} \left(u_{k,j} + u_{j,k} \right) \tag{26}$$

The strain caused by the adsorption of gas in the coal seam is volumetric strain and is spatially uniform. Based on the theory of elastic mechanics for porous media, considering the effects of geostress, gas pressure, thermal strain, and adsorption strain, the total strain of the coal body can be expressed as follows (Fan et al., 2019b; Li and Elsworth, 2019; Vishal et al., 2018):

$$\varepsilon_{kj} = \frac{1}{2G}\sigma_{kj} - \left(\frac{1}{6G} - \frac{1}{9K}\right)\sigma_{cc}\delta_{kj} + \frac{\alpha_{m}p_{m} + \alpha_{f}p_{f}}{3K}\delta_{kj} + \frac{\alpha_{T}T}{3}\delta_{kj} + \frac{\varepsilon_{m}^{s}}{3}\delta_{kj}$$
(27)

where *G* is the shear modulus of coal, GPa; *K* is the bulk modulus, MPa; δ_{kj} is the Kronecker delta with 1 for k = j and 0 for $k \neq j$.

Substituting Eqs. (26), and (27) into Eq. (25), the governing equation for the elastic deformation field of the coal body can be obtained as follows (Li et al., 2016; Zhou et al., 2023):

$$Gu_{k,jj} + \frac{G}{1 - 2v}u_{j,jk} - K\alpha_{T}T_{,k} - \alpha_{m}p_{m,k} - \alpha_{f}p_{f,k} - K\sum_{i=1}^{3} \varepsilon_{mi}^{S}, k + F_{k}$$

$$= 0$$
(28)

where v is poisson's ratio of coal.

2.5. THM model validation

2.5.1. Coupling relation of THM model

Eqs. (14), (19), (20) and (28) form a THM multi-field coupling mathematical model of GM-ECBM. These equations can quantitatively characterize the spatiotemporal evolution of the physical fields in the GM-ECBM process. Changes in both the matrix and fracture systems lead to variations in fracture porosity, gas adsorption/desorption, and diffusion. The fluid migration causes variation in effective stress, which in turn affects the coalbed's stress state and the temperature. The alteration in the coalbed stress state, in turn, induces changes in matrix porosity, fracture porosity/permeability, and generates strain energy that affects the temperature field. Similarly, the variation in coalbed temperature induces thermal stress and alters the gas adsorption/desorption rates. The coupled relationship is shown in Fig. 3, and is coupled through Eqs. (1), (9) and (10).

Considering the complexity of the THM coupling model,

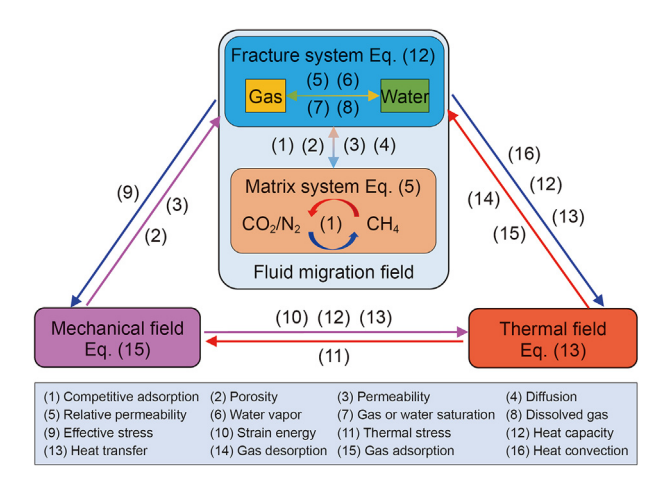


Fig. 3. The coupling relation of the proposed THM model.

obtaining an analytical solution is challenging. Therefore, we used COMSOL Multiphysics finite element software to solve it. First, the solid mechanics module was utilized to solve the mechanical field equations, capturing the deformation and stress distribution of the coal mass. Body forces were incorporated into the mechanical equations to describe the effects of fluid pressure, adsorption stress,

and thermal stress on coal deformation. The governing equations for fluid migration and temperature fields were modeled using the PDE module. Variables such as porosity, permeability, and relative permeability were defined and implemented through custom variable programming in COMSOL. An implicit coupling method was adopted, solving all coupled equations simultaneously, and the Newton-Raphson iterative algorithm was employed to ensure convergence among the physical fields.

2.5.2. THM model validation

The multi-field coupling experimental system for CH₄ displacement by gas injection in loaded coal was used to conduct a CO_2/N_2 displacement CH₄ experiment, as shown in Fig. 4(a). During the experiment, the axial stress was maintained at 8 MPa, and confining stress of 4 MPa, to test permeability. The system was vacuumed, and the CH₄ was injected into the core holder to be adsorbed in coal sample, followed by CO_2/N_2 (50%:50%) injection, the experimental flow is shown in Fig. 4(b). The CH₄ adsorption equilibrium pressure was 0.55 MPa (First, inject CH₄ into the adsorption tank using the CH₄ gas cylinder. After completing the injection, open the pressure regulator valve of the adsorption tank and adjust it until the pressure sensor displays a pressure of 0.55 MPa. Then allow the system to reach adsorption equilibrium). While the CO_2/N_2 injection pressure was maintained 0.7 MPa, the pressure at the outlet is standard atmospheric pressure. The

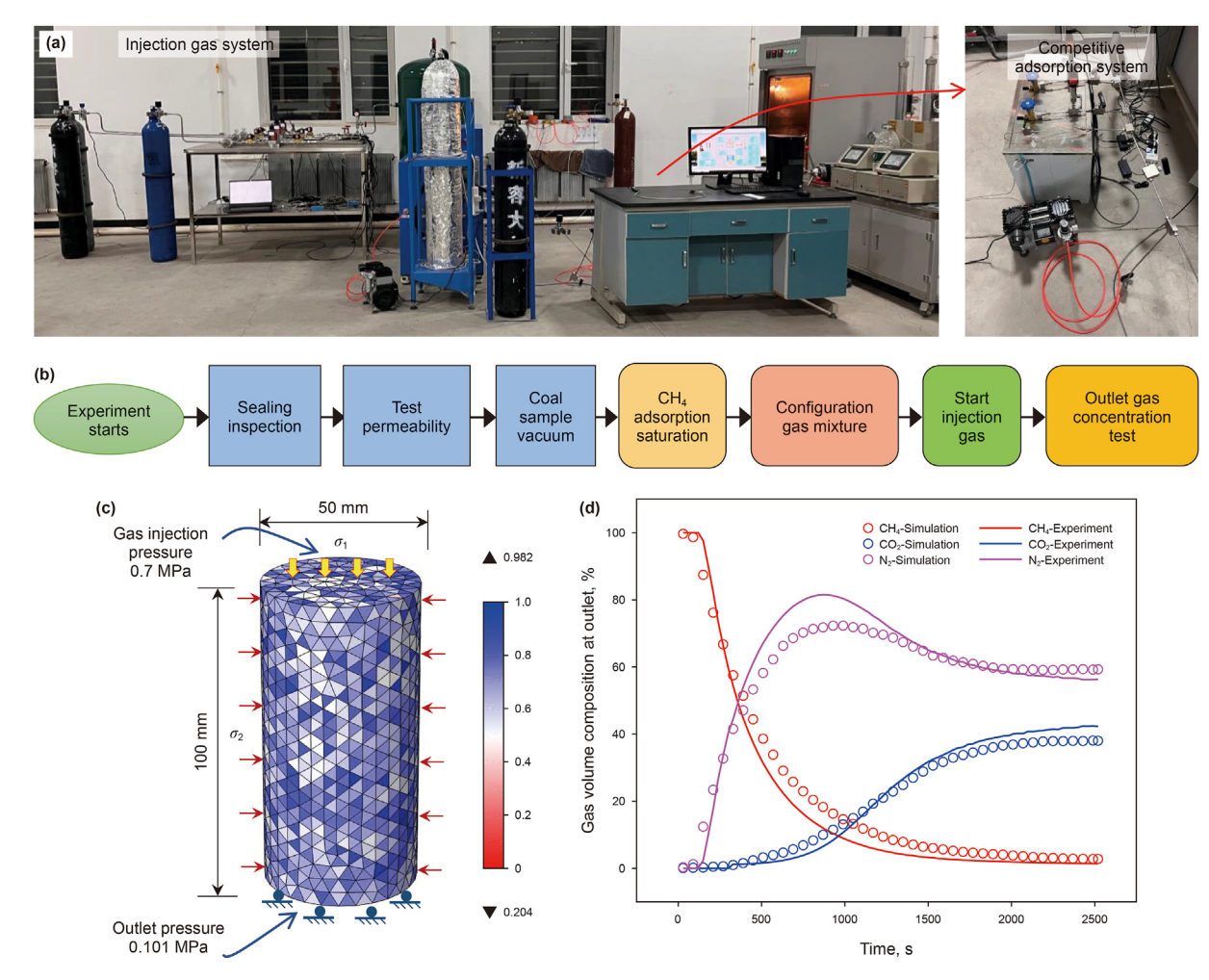


Fig. 4. (a) Multi-field coupling experimental system for CH₄ displacement by gas injection in loaded coal; (b) Experimental flow chart; (c) Geometric grid division and boundary condition; (d) Result comparison.

Table 2Key parameters used in model validation.

Parameter	Value	Source	Parameter	Value	Source
Elastic modulus of coal E, GPa	2.8	Experiments	Langmuir constant of CH ₄ adsorption strain ε_{L1}	0.0128	Zhou et al. (2013)
Poisson's ratio of coal v	0.32	Experiments	Langmuir pressure constant of CO ₂ P _{L2} , MPa	0.83	Experiments
Coal density ρ_c , kg/m ³	1480	Experiments	Langmuir volume constant of CO ₂ V _{L2} , m ³ /kg	0.0384	Experiments
Initial permeability k_0 , mD	0.4	Experiments	Dynamic viscosity of $CO_2 \mu_{g2}$, $Pa \cdot s$	1.34×10^{-5}	Fan et al. (2024)
Initial matrix porosity φ_{m0}	0.04	Wu et al. (2011)	Langmuir constant of CO_2 adsorption strain ε_{L2}	0.0362	Zhou et al. (2013)
Initial porosity of fracture φ_{f0}	0.018	Experiments	Langmuir pressure constant of N ₂ P _{L3} , MPa	1.61	Experiments
Langmuir pressure constant of $CH_4 P_{L1}$, MPa	1.21	Experiments	Langmuir volume constant of N ₂ V _{L3} , m ³ /kg	0.0180	Experiments
Langmuir volume constant of CH ₄ V _{L1} , m ³ /kg	0.0256	Experiments	Dynamic viscosity of $N_2 \mu_{g3}$, $Pa \cdot s$	1.84×10^{-5}	Fan et al. (2019a)
Dynamic viscosity of CH ₄ $\mu_{\rm g1}$, Pa·s	1.03×10^{-5}	Fan et al. (2019a)	Langmuir constant of N_2 adsorption strain ε_{L3}	0.0058	Zhou et al. (2013)

permeability is 0.4 mD, and the porosity is 0.018. Based on the results of the physical experiment, a core-scale GM-ECBM numerical simulation was conducted, with the geometric model and boundary conditions specified in Fig. 4(c), and key parameters listed in Table 2.

Fig. 4(d) illustrates the variations in the concentrations of CH₄, CO₂, and N₂ at the outlet, as observed in both simulation and experimental data. Initially, the gas composition at the outlet consisted of pure CH₄. Over time, the concentration of CH₄ began to decline, while the proportions of CO₂ and N₂ correspondingly rose. N₂ broke through the coal sample first, followed by CO₂. The overall trends observed in the numerical simulation were consistent with those measured in the experiment.

3. Numerical simulation of GM-ECBM recovery

3.1. Geometry model and boundary conditions

A traditional five-point well pattern was implemented, a geometric model with size of 200 m \times 200 m was established, as shown in Fig. 5. The diameter of the wells is 0.1 m. Roller boundary conditions were applied to the model's surrounding boundaries, with no fluid inflow or outflow on all sides. The initial conditions within the coalbed were specified as follows: CH₄ pressure is 5.24 MPa, CO₂ and N₂ pressures are 0.15 MPa, water saturation is 0.82, and temperature is 305.5 K. The injection conditions are as follows: CO₂/N₂ injection pressure is 8 MPa, injection temperature is 323 K, the ratio of CO₂ to N₂ is 20:80, and the PW pressure is 0.15 MPa. The triangular mesh can better handle complex

geometric structures and supports local adaptive mesh refinement, thereby improving simulation accuracy and computational efficiency. The model was divided into 1092 triangular grid elements and 140 edge elements, with an average element quality of 0.86. Reference line AB and point (P_1, P_2) are designated to monitor GMECBM variations. Key parameters for the simulation are listed in Table 3.

3.2. Results of GM-ECBM numerical simulations

3.2.1. Evolution of reservoir parameters

Fig. 6 presents the dynamic changes in coalbed key parameters along line AB in the GM-ECBM process. Fig. 6(a) details the evolution of gas content over time, revealing an expanding gradient of CO₂/N₂ migration within the coalbed as the duration of injection increases. The gas content is higher near the IW and diminishes towards the PW. Overall, gas content shows a decreasing trend with time. Fig. 6(b) shows reservoir pressure evolution, which is higher around the IW and lower near the PW. Initially, reservoir pressure near the PW decreases due to extraction effects, then gradually recovers as the injected gases reach the area. While the variation and causes of reservoir pressure near the IW are opposite to those near the PW. Fig. 6(c) indicates that reservoir temperature near the PW gradually decreases due to CH₄ desorption, whereas the temperature near the IW rises but within a limited range. Fig. 6(d) shows that permeability ratio near the PW decreases to about 0.90 within the first 1000 d, then gradually increases to reach 1.10 by around 3000 d. In contrast, the permeability ratio near the IW initially rises but then falls, influenced by the injected gases.

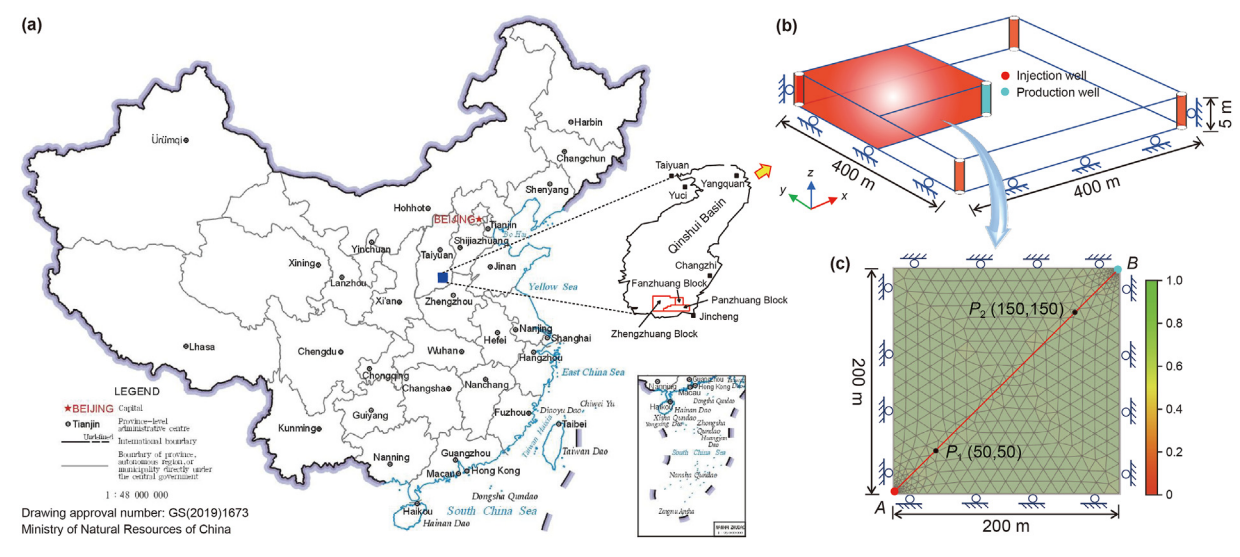


Fig. 5. Geometric model and the location of study area. (a) Qinshui Basin map; (b) Five-point well pattern; (c) Geometric model.

Table 3Key parameters for numerical simulation.

Parameter	Value	Source	Parameter	Value	Source
Poisson's ratio of coal v	0.35	Fan et al. (2019a)	Desorption time of $N_2 \tau_3$, d	4	Zhou et al. (2023)
Initial permeability k_0 , mD	1.0	Field data	Equal heat of adsorption of $N_2 q_{st3}$, kJ/mol	12.8	Fan et al. (2019a)
Specific heat capacity of coa C_s , $J/(kg \cdot K)$	1350	Li et al. (2016)	Specific heat capacity of $N_2 C_{g3}$, $J/(kg \cdot K)$	1040	Fan et al. (2019a)
Thermal conductivity of coal skeleton λ_s , W/(m·K)	0.1913	Li et al. (2016)	Thermal conductivity of $N_2 \lambda_{g3}$, $W/(m \cdot K)$	0.0262	Fan et al. (2019a)
Thermal expansion coefficient of coal skeleton α_T , 1/K	2.4×10^{-5}	Pan et al. (2020)	Dynamic viscosity of water μ_w , 10^{-3} Pa s	1.01	Pan et al. (2020)
Desorption time of $CH_4 \tau_1$, d	4.0	Zhou et al. (2022)	Specific heat capacity of water C_w , $J/(kg \cdot K)$	4187	Pan et al. (2020)
Equal heat of adsorption of $CH_4 q_{st1}$, kJ/mol	15.3	Zhou et al. (2022)	Relative permeability of water k_{rw0}	1.0	Yang et al. (2023)
Specific heat capacity of $CH_4 C_{g1}$, $J/(kg \cdot K)$	2220	Zhou et al. (2023)	The saturation of bound water s_{wr}	0.32	Fan et al. (2019a)
Thermal conductivity of $CH_4 \lambda_{g1}$, $W/(m \cdot K)$	0.0371	Zhou et al. (2023)	Relative permeability of gas k_{rg0}	0.875	Fan et al. (2019b)
Desorption time of $CO_2 \tau_2$, d	3.5	Zhou et al. (2023)	Klingberg factor b_k , MPa	0.76	Fan et al. (2019b)
Equal heat of adsorption of CO_2 q_{st2} , kJ/mol	19.2	Wang et al. (2015)	Temperature coefficient of gas c_1 , 1/K	0.021	Zhou et al. (2023)
Specific heat capacity of $CO_2 C_{g2}$, $J/(kg \cdot K)$	844	Fan et al. (2019b)	The pressure coefficient of a gas c_2 , 1/MPa	0.071	Zhou et al. (2023)
Thermal conductivity of $CO_2 \lambda_{g2}$, $W/(m \cdot K)$	0.0168	Fan et al. (2019b)	Capillary pressure p_{cgw} , MPa	0.035	Li et al. (2016)
Initial matrix porosity $arphi_{ m m0}$	0.045	Fan et al. (2024)	Initial matrix fracture $arphi_{ m fO}$	0.011	Fan et al. (2019b)

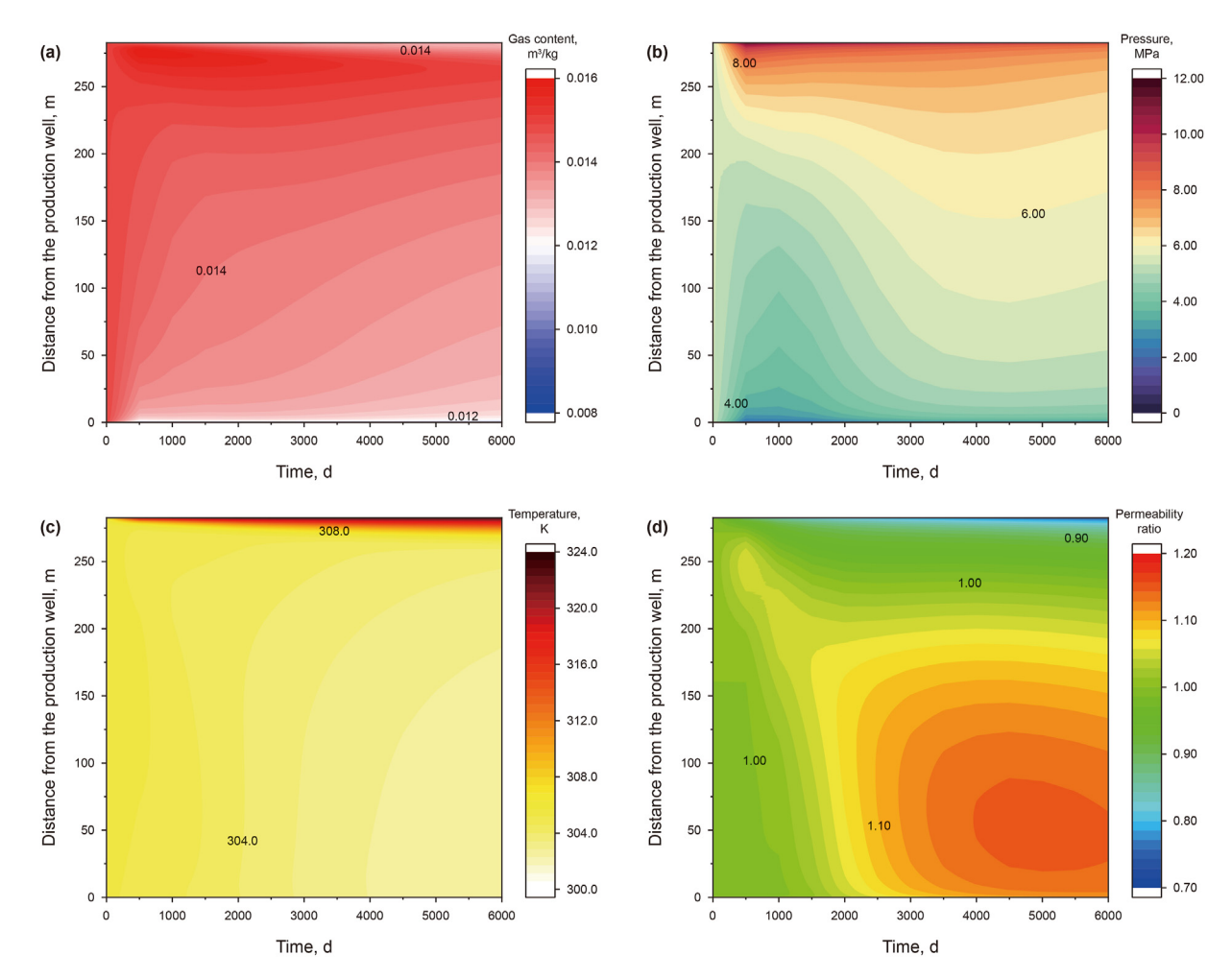


Fig. 6. Reservoir parameters in section A-B under GM-ECBM recovery conditions. (a) Gas content; (b) Gas pressure; (c) Temperature; (d) Permeability ratio.

3.2.2. Permeability evolution mechanism

Fig. 7 depicts the strain evolution and permeability-dominant mechanisms at points P_1 and P_2 during the GM-ECBM process. Positive strain represents coal mass shrinkage, while negative strain indicates expansion. As revealed in Fig. 7(a) and (b), coal deformation is chiefly influenced by gas adsorption/desorption and effective stress, with temperature having a relatively minor impact. At point P_1 (near the PW), the strain is largely due to CH₄ desorption, causing coal to shrinkage initially. During later stages, CO_2/N_2

adsorption gradually counteracts the shrinkage caused by CH_4 desorption, resulting in a slow increase in strain. Effective stress contributes to initial strain increases but stabilizes thereafter. At point P_2 (near the IW), gas adsorption/desorption strain is also initially dominated by CH_4 desorption. In the later stage, the strain gradually decreased due to CO_2/N_2 adsorption. The effective stress gradually decreases with the injection of gas, resulting in an increase in strain. However, during later stages, production-induced pressure depletion slightly raises effective stress, causing a minor

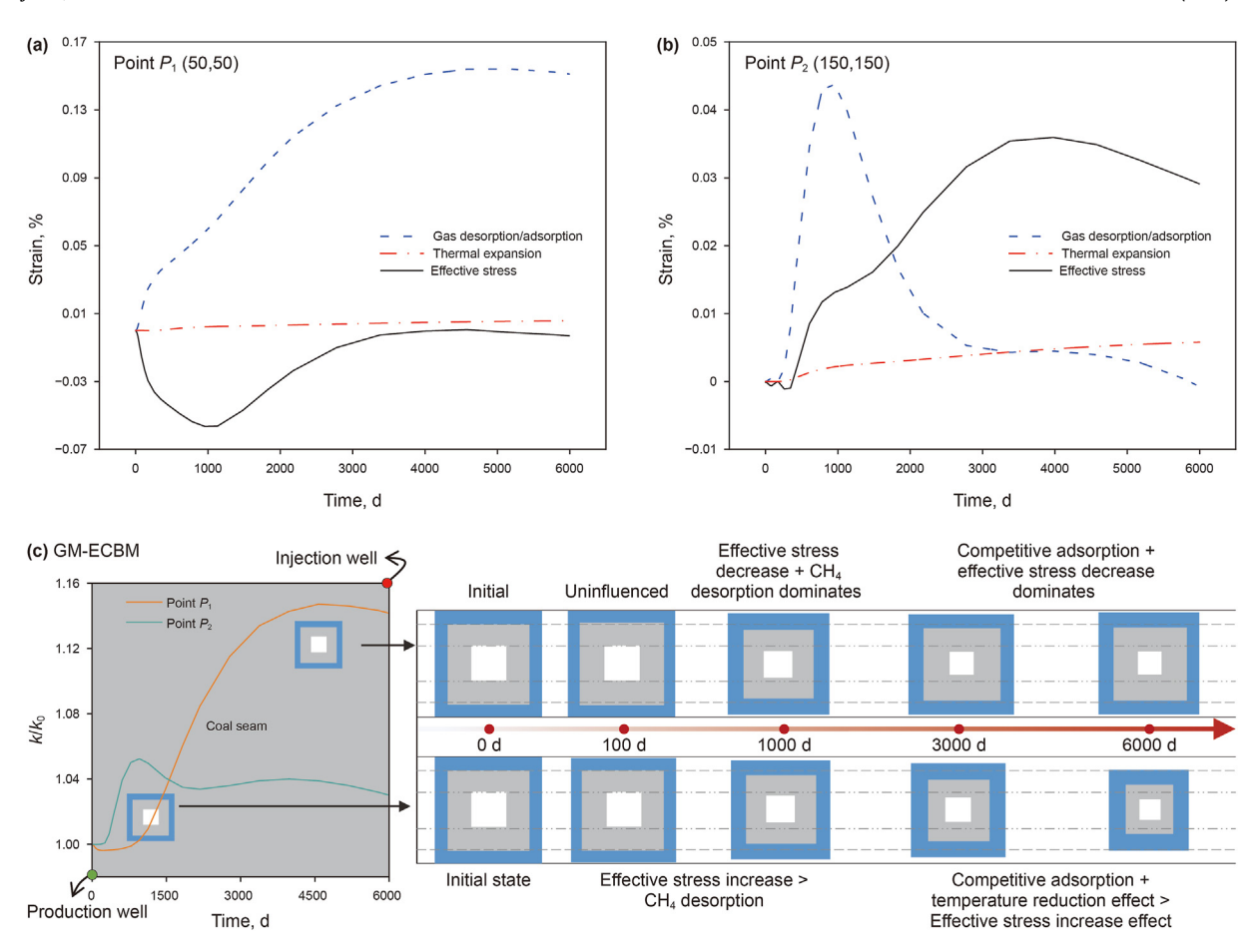


Fig. 7. Evolution of strain and permeability mechanism in GM-ECBM with time.

decrease in strain. The permeability evolution mechanisms at points P_1 and P_2 can be divided into two stages, with differences in dominant factors and timing, as shown in Fig. 7(c). At point P_1 , permeability in the initial phase (0–1000 d) is mainly influenced by the effective stress increase, which leads to decreased permeability. In the later stage, CH₄ desorption gradually leads to permeability increase. At point P_2 , the early stage is divided into two phases: 0–100 d, there is no significant change in permeability because it is far from both the PW and the IW. 100–1000 d, the permeability

increases mainly due to the reduction in effective stress. While in the later phases, permeability remains relatively stable, influenced by a combination of competitive adsorption and effective stress reduction.

3.2.3. Gas production and injection characteristics

Fig. 8(a) is the gas production/injection rates during conventional production and GM-ECBM. The CH₄ production rate shows an increasing-decreasing-increasing-decreasing trend. The first

5000

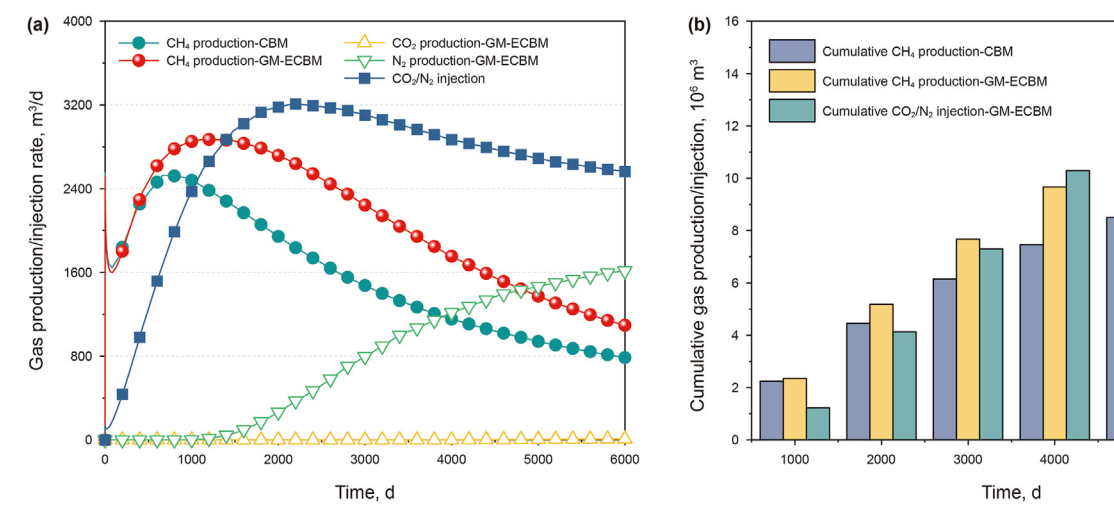


Fig. 8. Gas production and injection during conventional production and GM-ECBM. (a) Gas production and injection rate; (b) Cumulative gas production and injection.

peak production rate may result from the rapid release of free gas in the coal seam near the PW with the second liberated by dewatering. During GM-ECBM, the CH4 production rate significantly increases compared to conventional production, and the peak production period lasts longer. The CH₄ production peak during conventional production occurs on the 664 d, with a value of 2528.7 m³/d. During GM-ECBM, the CH₄ production peak occurs on the 1132 d, with a value of 2895.7 m³/d, an increase of 16.63% compared to conventional production. CO₂ and N₂ break through on the 3920 and 960 d, respectively. After breakthrough, the N₂ production rate increases rapidly, while the CO₂ production rate stays consistently low. The main reason is the relatively low injection ratio of CO₂ and its strong adsorption capacity on coal. The injected CO₂ is primarily adsorbed in the coal matrix, while the CO₂ content in the fractures is relatively low. The injection rate of the CO_2/N_2 mixture initially increases and subsequently decreases.

Fig. 8(b) presents the cumulative gas production/injection during conventional production and GM-ECBM. The cumulative CH₄ production and the CO₂/N₂ injection both exhibit a linear upward trend, with the cumulative CH₄ production during GM-ECBM being significantly greater than during conventional production. After 6000 d of operation, the cumulative CH₄ production is 9.36×10^6 m³ during conventional production, while the cumulative CH₄ production is 12.45×10^6 m³ during GM-ECBM, an increase of 32.98% compared to conventional production. The cumulative CO₂/N₂ injection volume is 15.69×10^6 m³ during GM-ECBM.

3.3. Influence of geological parameters on GM-ECBM

The sensitivity of CH₄ production and mixed gas injection rates to geological parameters s in the GM-ECBM process is crucial for optimizing injection strategies and enhancing CH₄ recovery efficiency. In this study, we define the time at which CO_2/N_2 production rates reach 50% of the CH₄ production rate as the operating duration, with a maximum operating duration of 6000 d within this study scale. The CH₄ production and CO_2/N_2 injection achieved within this operating duration are considered effective CH₄ production and CO_2/N_2 injection.

3.3.1. Gas production rate under different geological parameters

As the permeability increases, the CH₄ production rate also rises, with the peak occurring earlier, but the later decay is also more rapid. Similarly, the CO₂/N₂ mixture production rate increases, as present in Fig. 9(a). When the permeability is 0.6, 0.8, 1.0, and 1.2 mD, the peaks of CH₄ production rate reach 1978.9, 2473.1, 2895.7, and 3262.9 m³/d, respectively. At higher coal seam temperature, the CH₄ production rate decreases, and the peak appears earlier, whereas CO₂/N₂ mixture production rate tends to increase, as shown in Fig. 9(b). This is mainly because elevated temperatures reduce gas adsorption capacity and increase molecular mobility. Greater matrix porosity promotes CH₄ desorption and diffusion and enhances CO₂/N₂ adsorption and diffusion. Consequently, higher matrix porosity leads to an increase in CH₄ production rate and a reduce in CO_2/N_2 mixture production rate, as illustrated in Fig. 9(c). Initial water saturation primarily affects early stages of GM-ECBM. Fig. 9(d) shows that higher water saturation prolongs the coal seam dewatering phase, causing a gradual decline in the gas production rate. The higher initial CH4 pressures increase CH4 production rate and cause earlier peak appearances. The effect on the production rate of CO₂/N₂ mixture is small, mainly because the CO₂/ N₂ production rate decreases in the later period due to the rise in initial CH_4 pressure, as shown in Fig. 9(e).

3.3.2. CO₂/N₂ injection rate under different geological parameters

As the permeability increases, the CO₂/N₂ injection rate significantly improves, as shown in Fig. 10(a). This indicates that higher permeability facilitates gas seepage and injection, achieving injection targets more effectively. Under all permeability conditions, there is no noticeable decline in the injection rate with time. In contrast, as the temperature increases, the CO₂/N₂ injection rate gradually decreases, as illustrated in Fig. 10(b). Elevated temperatures reduce coal seam permeability and gas adsorption capacity, making it more difficult to sustain high CO₂/N₂ injection rate in high-temperature environments. With increasing matrix porosity, the CO₂/N₂ injection rate also increases, as shown in Fig. 10(c). Higher matrix porosity provides more storage space, facilitating gas injection and diffusion. Water in the coal seam occupies fracture spaces, obstructing gas seepage and reducing injection rate, especially during the early stages. As the initial water saturation increases, the CO₂/N₂ injection rate gradually decreases, as present in Fig. 10(d). The variation in initial CH₄ pressure has a minimal impact on the CO_2/N_2 injection rate, as shown in Fig. 10(e).

3.3.3. Sensitivity analysis

The operating duration of GM-ECBM under different geological parameters, as well as the cumulative CH₄ production and CO₂/N₂ injection over this period, were statistically analyzed, as shown in Fig. 11. Overall, as the coal permeability and temperature increase, the operating duration of GM-ECBM gradually shortens, while it extends with increases in matrix porosity, initial water saturation, and CH₄ pressure. With the increases in coal permeability, temperature, and initial CH₄ pressure, the cumulative CH₄ production gradually increases, but declines with the rises of coalbed temperature and water saturation. The cumulative CO₂/N₂ injection increases with the rises of coal permeability, matrix porosity and initial CH₄ pressure, but decreases as the coalbed temperature and initial water saturation increase.

A sensitivity analysis is conducted on the impact of key geological parameters in GM-ECBM. The analysis method is as follows: By calculating the ratio of the adjacent independent variables (dimensionless) to the corresponding dependent variables (cumulative CH₄ production or cumulative CO₂/N₂ injection), the corresponding score points are obtained, and the average score points for each geological condition is calculated. The influence of different geological parameters on cumulative CH₄ production or cumulative CO₂/N₂ injection is assessed using the average score points, as shown in Fig. 12. The impact of geological parameters on cumulative CH₄ production is ranked as follows: initial gas pressure, coalbed permeability, coalbed temperature, initial water saturation, matrix porosity. The influence on cumulative CO₂/N₂ injection are ranked as follows: coalbed permeability, coalbed temperature, initial water saturation, initial gas pressure, matrix porosity.

4. Discussion

4.1. Variation of coalbed permeability with depth

Sensitivity analysis reveals that permeability significantly impacts GM-ECBM. Therefore, the injection ratio of CO_2/N_2 under varying permeability conditions in the GM-ECBM process requires further investigation. The Qinshui Basin and Ordos Basin are important CBM production areas in China. The relationship between coalbed depth and permeability in these regions was analyzed, as shown in Fig. 13. It was observed that the permeability decreases linearly with increasing coalbed burial depth. The permeability in the study areas was categorized into three levels: low permeability ($k_0 \leq 0.5$ mD), medium permeability (0.5

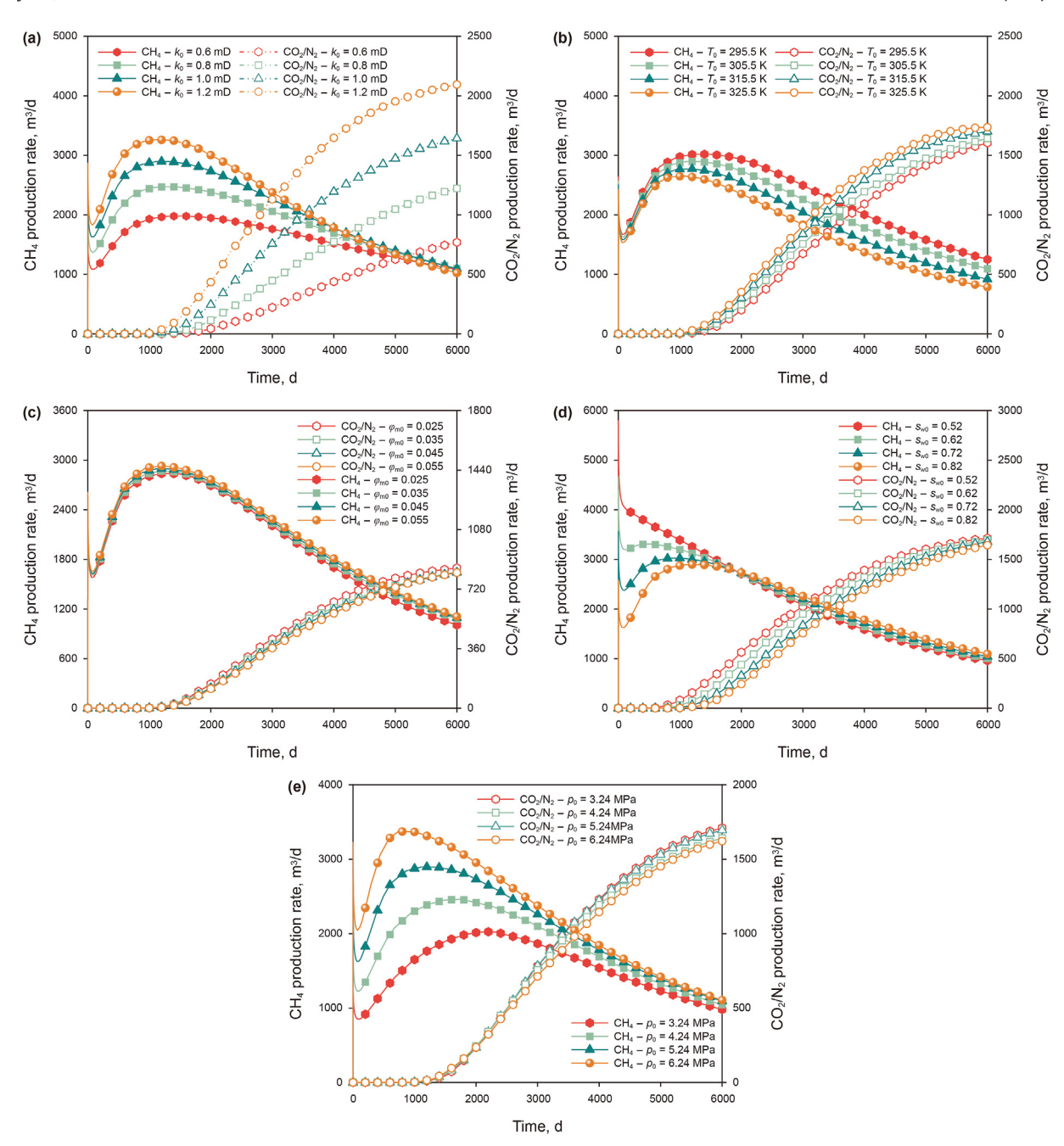


Fig. 9. Gas production rates under different geological parameters. (a) Coal permeability; (b) Coal temperature; (c) Coal matrix porosity; (d) Initial water saturation; (e) Varying initial CH₄ pressure.

mD < $k_0 \leq 1.0$ mD), and high permeability ($k_0 > 2.0$ mD). The appropriate CO_2/N_2 injection ratio for the GM-ECBM was investigated for different permeability category.

4.2. Optimization composition determination

Fig. 14(a)—(c) shows the CH₄ and CO_2/N_2 mixture production rate under different permeability and CO_2/N_2 injection composition. As the permeability increases, the CH₄ and CO_2/N_2 mixture production rate decreases. At a constant injection composition, higher permeability results in an earlier occurrence of CH₄ production rate peak. Under high permeability conditions, injecting a higher N_2 composition results in an excessively short operating

duration for GM-ECBM, while low permeability conditions more suitable for injecting a higher composition of N₂.

The operating duration of GM-ECBM under different permeability and CO_2 composition is shown in Fig. 14(d). As the permeability and N_2 composition increase, the operating duration also gradually increases. This is primarily because the injection $\mathrm{CO}_2/\mathrm{N}_2$ is more easily transport from the IW to the PW under the high permeability, and N_2 has weaker adsorption in the coalbed compared to CH_4 and CO_2 , making a higher N_2 composition more likely to break through.

Cumulative CH₄ production under different permeability and CO₂ composition is shown in Fig. 14(e). Under low and medium permeability conditions, the cumulative CH₄ production initially

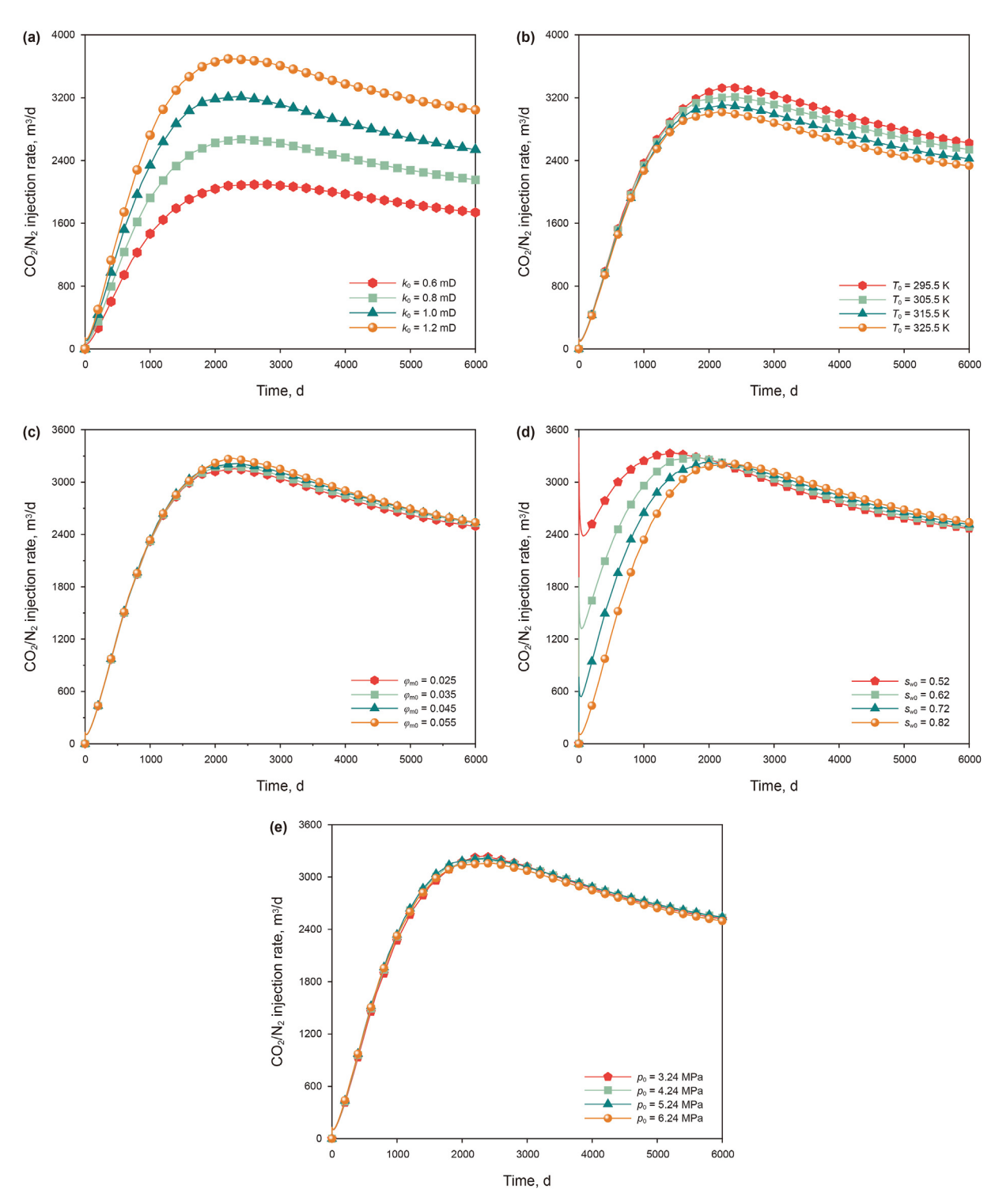


Fig. 10. CO₂/N₂ injection rates under varying geological parameters. (a) Coal permeability; (b) Coal temperature; (c) Coal matrix porosity; (d) Initial water saturation; (e) Varying initial CH₄ pressure.

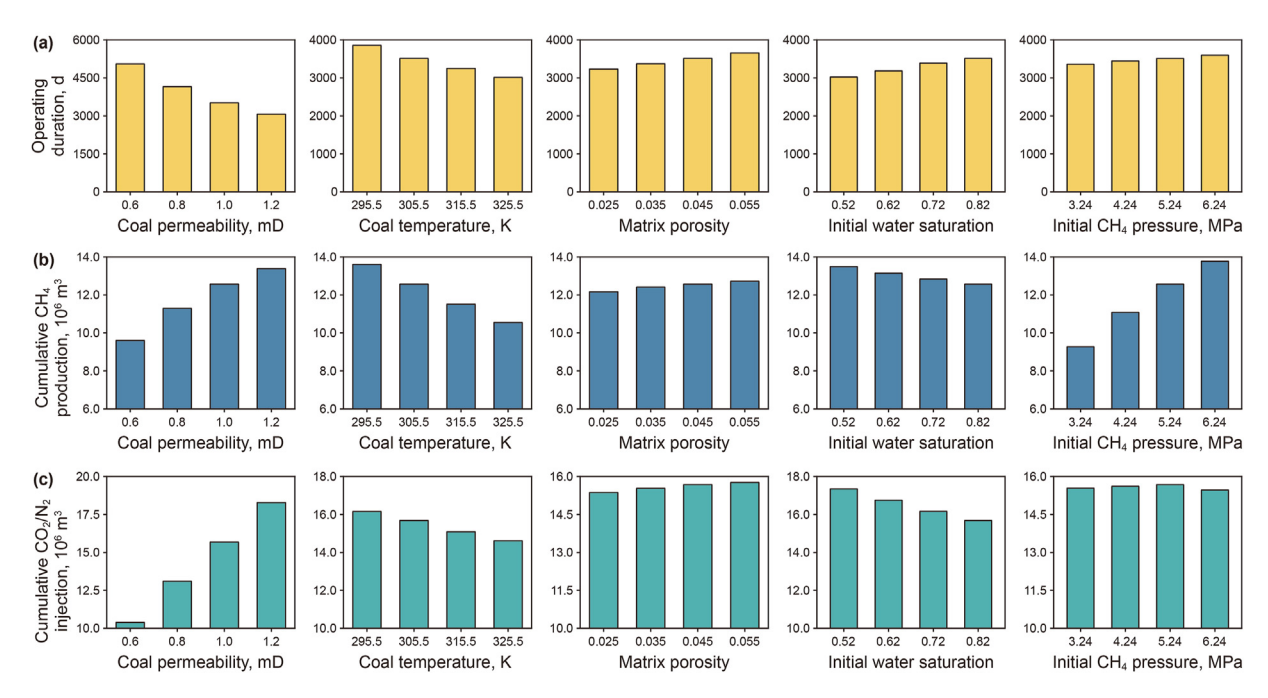


Fig. 11. (a) Operating duration; (b) Cumulative CH₄ production; (c) Cumulative CO₂/N₂ injection.

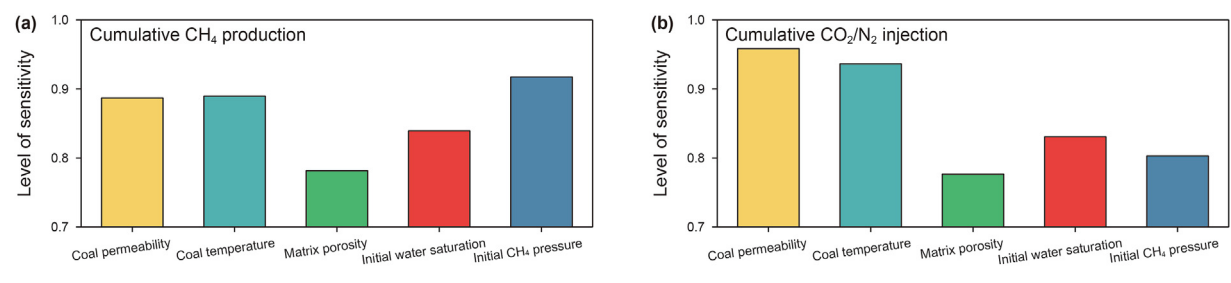


Fig. 12. Sensitivity of geological parameters in GM-ECBM process.

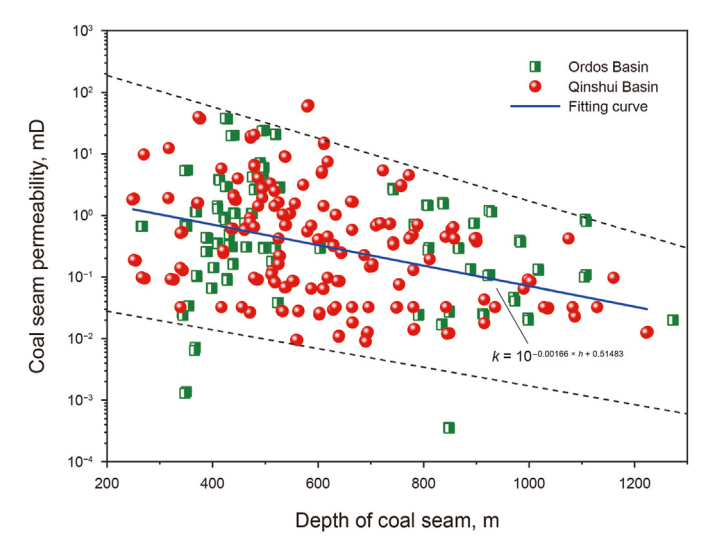


Fig. 13. Relationship between coalbed depth and permeability.

increases and then decreases as the CO₂ composition increases. Under high permeability conditions, the cumulative CH₄ production shows a rapid initial increase followed by a slower one. For low and medium permeability coalbeds, a high N₂ composition

injection can increase reservoir permeability, but too high N_2 composition may likely cause early N_2 breakthrough. In high permeability coalbeds, N_2 tends to breakthrough quickly, therefore, injecting a high composition CO_2 can more fully displace CH_4 and increase cumulative CH_4 production. The injection optimal ratio of CO_2/N_2 is negatively correlated with coalbed permeability. That the optimal CO_2 injection ratios for low ($k_0 = 0.5 \, \text{mD}$), medium ($k_0 = 1.0 \, \text{mD}$) and high permeability ($k_0 = 2.0 \, \text{mD}$) coalbeds are 20%, 40%, and 100%, respectively.

4.3. Influence mechanism of permeability on gas mixture injection components

As shown in Fig. 15(a), under conditions of low permeability and high CO₂ composition, the fractures within the coal seam are relatively small, which restricts gas flow. The high CO₂ composition leads to a more pronounced matrix adsorption swelling effect, which further compresses the fracture width, resulting in even lower permeability and limiting the flow of CO₂/N₂ mixed gases into deep coal seam regions, thereby reducing CH₄ replacement rates and suppressing production. In contrast, when injecting high CO₂ composition into high-permeability coal seam, although CO₂ adsorption leads to matrix swelling and local permeability reduction, the naturally high permeability of the coal seam mitigates

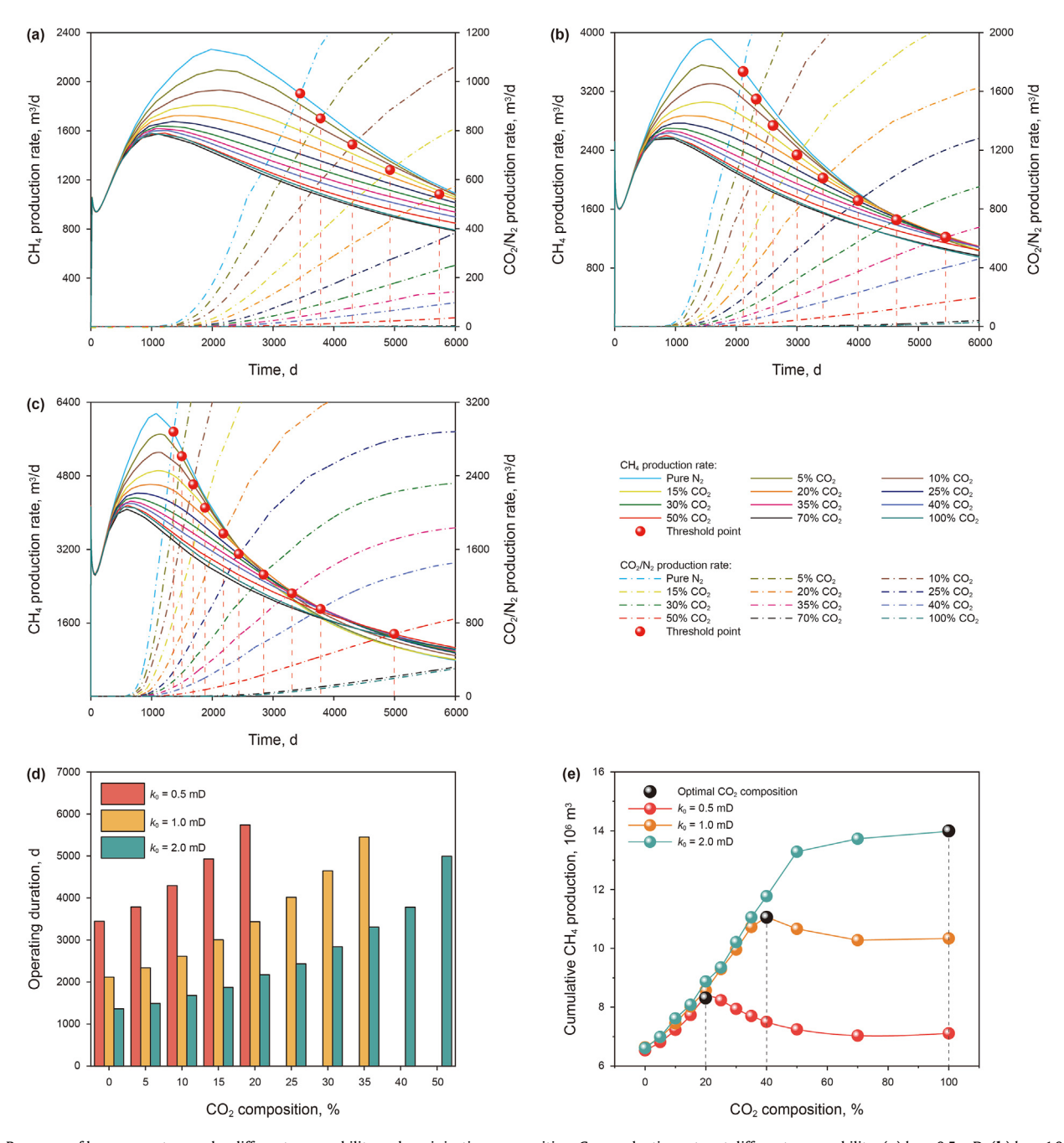


Fig. 14. Response of key parameters under different permeability and gas injection composition. Gas production rates at different permeability: (a) $k_0 = 0.5 \text{ mD}$; (b) $k_0 = 1.0 \text{ mD}$; (c) $k_0 = 2.0 \text{ mD}$. (d) Operating duration. (e) Cumulative CH₄ production.

rapid CO_2/N_2 gas breakthrough to some extent, as shown in Fig. 15(b). Under low-permeability and low CO_2 composition conditions, the adsorption swelling effect of CO_2 is relatively weak. The width of fractures increases under the effective stress action, indirectly enhancing the displacement effect of the mixed gas, as illustrated in Fig. 15(c). In high-permeability and low CO_2 composition conditions, due to the lower dynamic viscosity and weaker adsorption properties of N_2 , and the high N_2 composition can further increase the permeability, leading to the rapid breakthrough of N_2 into PW, as in Fig. 15(d).

5. Conclusions

An improved THM coupling model was proposed by considering non-isothermal ternary gases adsorption, dynamic evolution of matrix and fractures, gas dissolution in water, gas—water two-phase seepage. The model was initially validated and subsequently utilized in GM-ECBM simulation. The analysis covered the impact of key geological parameters on GM-ECBM performance, and revealed the influence mechanism of permeability on the $\rm CO_2/N_2$ injection ratio. The key conclusions are as follows:

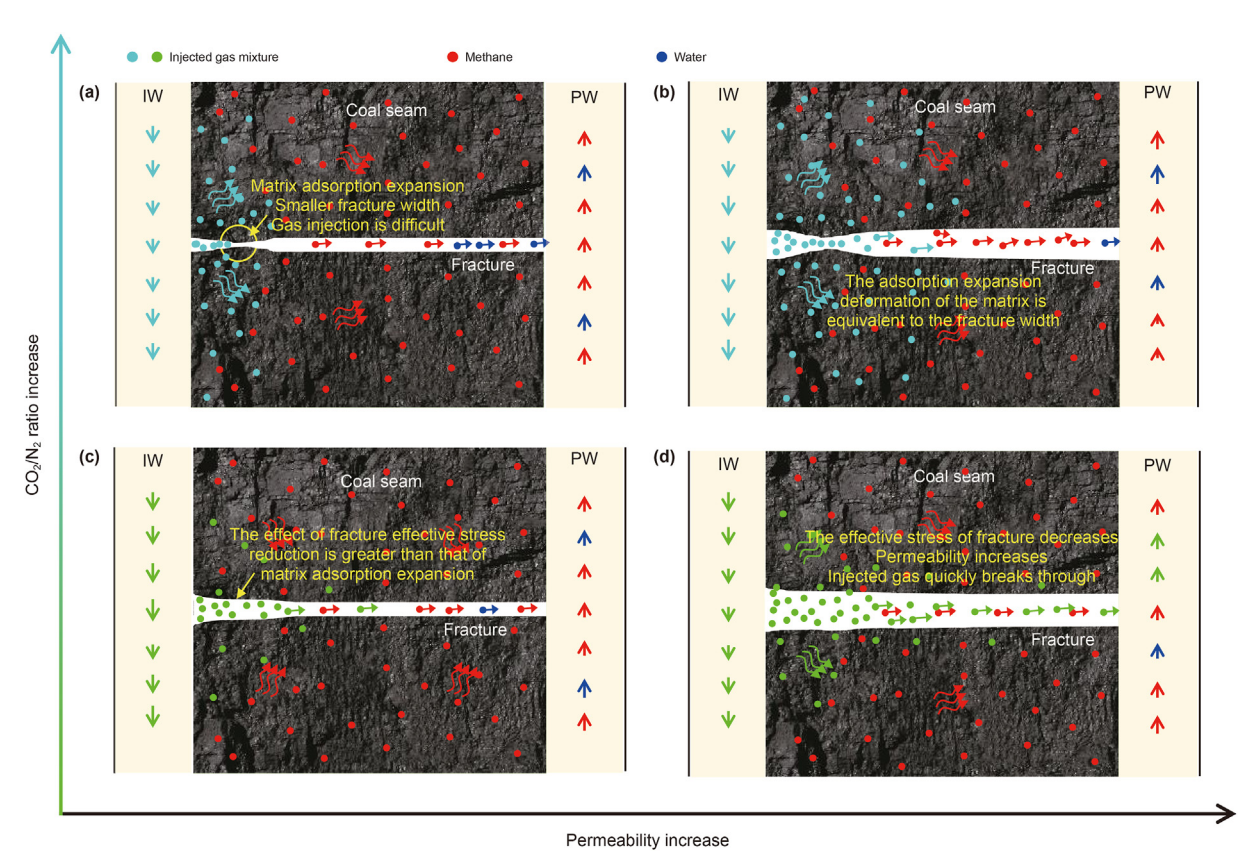


Fig. 15. Relationship between permeability and injected CO₂/N₂ composition.

- (1) During the GM-ECBM process, the permeability is mainly influenced through the dual effects of gas adsorption/ desorption and effective stress, which generally shows an increase trend. Near PW, permeability initially decreases due to effective stress increases, and subsequently rises due to CH₄ desorption. Near the IW, permeability initially increases due to reduced effective stress and later stabilizes under the combined influence of CO₂/N₂ adsorption and effective
- (2) Higher permeability and matrix porosity promote CH₄ production and CO₂/N₂ mixture injection. Higher temperature and water saturation reduce CH₄ production and CO₂/N₂ injection. Higher CH₄ pressure aids in improving CH₄ production but has a minimal impact on the CO₂/N₂ injection. Increases in temperature and permeability shorten the operating duration of GM-ECBM, while increases in matrix porosity, water saturation, and CH₄ pressure extend the operating duration.
- (3) The influence of geological parameters on cumulative CH₄ production is ranked as follows: CH₄ pressure, permeability, temperature, water saturation, and matrix porosity. The influence on cumulative CO₂/N₂ injection is ranked as follows: initial permeability, temperature, water saturation, CH₄ pressure, and matrix porosity.
- (4) Under low-permeability conditions, injecting a high CO₂ composition tends to induce matrix swelling, limiting permeability. Thus, a higher N₂ composition should be injected to improve coal seam permeability and displacement efficiency. In high-permeability coal seams, the matrix swelling effect induced by high CO₂ composition helps to moderate the rapid breakthrough of CO₂/N₂ mixed gases, allowing sufficient CH₄ displacement and enhancing CH₄

production. Within this research, the optimal CO₂ composition in low, medium, and high permeability coal seams was found to be 20%, 40%, and 100%, respectively.

The established THM coupling model is based on that the coal seam is assumed as a homogeneous and isotropic media, and the chemical reactions of minerals, e.g. dissolution and precipitation, are ignored. Additionally, the geometry of fractures, including fracture length and direction, plays a significant role in gas flow. Future studies will explore the integration of these factors into the THM coupling model to address the current limitations. The above aspects will be the focus of upcoming research.

CRediT authorship contribution statement

Lei Yang: Writing — original draft, Software, Methodology, Formal analysis, Conceptualization. **Chao-Jun Fan:** Writing — original draft, Visualization, Supervision, Resources, Project administration, Methodology, Funding acquisition, Conceptualization. **Ming-Kun Luo:** Validation, Supervision, Data curation. **Hai-Ou Wen:** Validation, Data curation. **Hao Sun:** Writing — review & editing, Software. **Li-Jun Zhou:** Writing — review & editing, Validation. **Zhi-Heng Cheng:** Validation, Supervision. **Ze-Peng Zhang:** Writing — review & editing.

Declaration of competing interest

The authors declare that they have no known competing financial interests or personal relationships that could have appeared to influence the work reported in this paper.

Acknowledgement

This research was financially supported by the National Natural Science Foundation of China (Grant No. 52174117), the University-local Government Scientific and Technical Cooperation Cultivation Project of Ordos Institute-LNTU (Grant No. YJY-XD-2024-A-009), the Basic Scientific Research Project of Liaoning Provincial Department of Education (Grant No. JYTZD2023073), the Liaoning Revitalization Talents Program (XLYC2203139), the Liaoning Provincial Natural Science Foundation Program (Excellent Youth Fund) (Grant No. 2024JH3/10200043).

References

- Asif, M., Wang, L., Naveen, P., et al., 2024. Influence of competitive adsorption, diffusion, and dispersion of CH₄ and CO₂ gases during the CO₂-ECBM process. Fuel 358, 130065. https://doi.org/10.1016/j.fuel.2023.130065.
- Dai, L.P., Pan, Y.S., Xiao, Y.H., et al., 2024. Parameter design method for destressing boreholes to mitigate roadway coal bursts: Theory and verification. Rock Mech. Rock Eng. 1–18. https://doi.org/10.1007/s00603-024-04042-x.
- Du, S.Y., Wang, M.Z., Yang, J.S., et al., 2023. An enhanced prediction framework for coalbed methane production incorporating deep learning and transfer learning. Energy 282, 128877. https://doi.org/10.1016/j.energy.2023.128877.
- Durucan, S., Ahsan, M., Syed, A., et al., 2013. Two phase relative permeability of gas and water in coal for enhanced coalbed methane recovery and CO₂ storage. Energy Proc. 37, 6730–6737. https://doi.org/10.1016/j.egypro.2013.06.606.
- Fan, C.J., Elsworth, D., Li, S., et al., 2019a. Modelling and optimization of enhanced coalbed methane recovery using CO₂/N₂ mixtures. Fuel 253, 1114–1129. https:// doi.org/10.1016/j.fuel.2019.04.158.
- Fan, C.J., Elsworth, D., Li, S., et al., 2019b. Thermo-hydro-mechanical-chemical couplings controlling CH₄ production and CO₂ sequestration in enhanced coalbed methane recovery. Energy 173, 1054–1077. https://doi.org/10.1016/ j.energy.2019.02.126.
- Fan, C.J., Yang, L., Sun, H., et al., 2023a. Recent advances and perspectives of CO₂-enhanced coalbed methane: Experimental, modeling, and technological development. Energy Fuels 37 (5), 3371–3412. https://doi.org/10.1021/acs.energyfuels.2c03823.
- Fan, C.J., Xu, L.J., Elsworth, D., et al., 2023b. Spatial—temporal evolution and countermeasures for coal and gas outbursts represented as a dynamic system. Rock Mech. Rock Eng. 56 (9), 6855–6877. https://doi.org/10.1007/s00603-023-03429-6
- Fan, N., Wang, J.R., Deng, C.B., et al., 2020. Numerical study on enhancing coalbed methane recovery by injecting N₂/CO₂ mixtures and its geological significance. Energy Sci. Eng. 8 (4), 1104–1119. https://doi.org/10.1002/ese3.571.
- Fan, Z.L., Zhang, D.S., Fan, G.W., et al., 2021. Non-Darcy thermal-hydraulic-mechanical damage model for enhancing coalbed methane extraction. J. Nat. Gas Sci. Eng. 93, 104048. https://doi.org/10.1016/j.jngse.2021.104048.
- Fan, Z.L., Fan, G.W., Zhang, D.S., et al., 2024. Modelling of flue gas injection and collaborative optimization of multi-injection parameters for efficient coalbased carbon sequestration combined with BP neural network parallel genetic algorithms. Fuel 368, 131536. https://doi.org/10.1016/j.fuel.2024.131536.
- Fang, H.H., Wang, Z.F., Sang, S.X., et al., 2023. Numerical analysis of matrix swelling and its effect on microstructure of digital coal and its associated permeability during CO₂-ECBM process based on X-ray CT data. Pet. Sci. 20 (1), 87–101. https://doi.org/10.1016/j.petsci.2022.07.011.
- Fang, H.H., Sang, S.X., Wang, Z.F., et al., 2024. Numerical analysis of temperature effect on CO₂ storage capacity and CH₄ production capacity during the CO₂-ECBM process. Energy 289, 130022. https://doi.org/10.1016/ j.energy.2023.130022.
- Fujioka, M., Yamaguchi, S., Nako, M., 2010. CO₂-ECBM field tests in the ishikari coal basin of Japan. Int. J. Coal Geol. 82 (3–4), 287–298. https://doi.org/10.1016/ j.coal.2010.01.004.
- Fujioka, M., Furukawa, H., Nako, M., 2008. The outcome of CO₂-ECBM Yubari pilot test. Journal of MMIJ 124 (12), 890–897. https://doi.org/10.2473/ journalofmmij.124.890.
- Huo, B.J., Jing, X.D., Fan, C.J., et al., 2019. Numerical investigation of flue gas injection enhanced underground coal seam gas drainage. Energy Sci. Eng. 7 (6), 3204–3219. https://doi.org/10.1002/ese3.491.
- Li, S., Fan, C.J., Han, J., Luo, M.K., et al., 2016. A fully coupled thermal-hydraulic-mechanical model with two-phase flow for coalbed methane extraction. J. Nat. Gas Sci. Eng. 33, 324–336. https://doi.org/10.1016/j.jngse.2016.05.032.
- Li, S., Qin, Y., Tang, D.Z., et al., 2023. A comprehensive review of deep coalbed methane and recent developments in China. Int. J. Coal Geol., 104369 https:// doi.org/10.1016/j.coal.2023.104369.
- Li, Z.W., Yu, H.J., Bai, Y.S., et al., 2023. Numerical study on the influence of temperature on CO₂-ECBM. Fuel 348, 128613. https://doi.org/10.1016/j.fuel.2023.128613.
- Li, Z.Y., Elsworth, D., 2019. Controls of CO₂–N₂ gas flood ratios on enhanced shale gas recovery and ultimate CO₂ sequestration. J. Petrol. Sci. Eng. 179, 1037–1045. https://doi.org/10.1016/j.petrol.2019.04.098.

Lin, J., Ren, T., Wang, G., et al., 2018. Simulation investigation of N₂-injection enhanced gas drainage: Model development and identification of critical parameters. J. Nat. Gas Sci. Eng. 55, 30–41. https://doi.org/10.1016/i.jngse.2018.04.016.

- Liu, J., Xie, L.Z., Elsworth, D., et al., 2019. CO₂/CH₄ competitive adsorption in shale: Implications for enhancement in gas production and reduction in carbon emissions. Environ. Sci. Technol. 53 (15), 9328–9336. https://doi.org/10.1021/ acs.est.9b02432.
- Liu, T., Shi, Y., Liu, T., et al., 2024. Dynamic response of gas recovery enhancement efficiency in coalbed methane displacement by hot flue gas: From the perspective of thermo-hydro-mechanical-chemical coupling. Energy Fuels 38 (8), 6962–6981. https://doi.org/10.1021/acs.energyfuels.4c00857.
- Liu, X.D., Sang, S.X., Zhou, X.Z., et al., 2023a. Coupled adsorption-hydro-thermomechanical-chemical modeling for CO₂ sequestration and well production during CO₂-ECBM. Energy 262, 125306. https://doi.org/10.1016/j.energy.2022.125306.
- Liu, X.D., Sang, S.X., Zhou, X.Z., et al., 2023b. Modelling of geomechanical response for coal and ground induced by CO₂-ECBM recovery. J. Nat. Gas Sci. Eng. 113, 204953. https://doi.org/10.1016/j.jgsce.2023.204953.
 Liu, Z.D., Lin, X.S., Zhu, W.C., et al., 2023. Effects of coal permeability rebound and
- Liu, Z.D., Lin, X.S., Zhu, W.C., et al., 2023. Effects of coal permeability rebound and recovery phenomenon on CO₂ storage capacity under different coalbed temperature conditions during CO₂-ECBM process. Energy 284, 129196. https:// doi.org/10.1016/j.energy.2023.129196.
- Ma, H.M., Yang, Y., Zhang, Y.M., et al., 2022. Optimized schemes of enhanced shale gas recovery by CO₂-N₂ mixtures associated with CO₂ sequestration. Energy Convers. Manag. 268, 116062. https://doi.org/10.1016/j.enconman.2022.116062.
- Ma, T.R., Rutqvist, J., Oldenburg, C.M., et al., 2017. Coupled thermal—hydrological—mechanical modeling of CO₂-enhanced coalbed methane recovery. Int. J. Coal Geol. 179, 81–91. https://doi.org/10.1016/j.coal.2017.05.013.
- Ma, T.R., Jiang, L.T., Shen, W.J., et al., 2023. Fully coupled hydro-mechanical modeling of two-phase flow in deformable fractured porous media with discontinuous and continuous Galerkin method. Comput. Geotech. 164, 105823. https://doi.org/10.1016/j.compgeo.2023.105823.
- Masoudian, M., 2016. Multiphysics of carbon dioxide sequestration in coalbeds: A review with a focus on geomechanical characteristics of coal. J. Rock. Mech. Geotech. 8, 93–112. https://doi.org/10.1016/j.jrmge.2015.08.002.
- Mwakipunda, C., Wang, Y.T., Mgimba, M.M., et al., 2023. Recent advances in carbon dioxide sequestration in deep unmineable coal seams using CO₂-ECBM technology: Experimental Studies, Simulation, and Field Applications. Energy Fuels 37 (22), 17161–17186. https://doi.org/10.1021/acs.energyfuels.3c03004.
- Meng, M., Qiu, Z.S., Zhong, R.Z., et al., 2019. Adsorption characteristics of supercritical CO₂/CH₄ on different types of coal and a machine learning approach. Chem. Eng. J. 368, 847–864. https://doi.org/10.1016/j.cej.2019.03.008.
- Mukherjee, M., Misra, S., 2018. A review of experimental research on Enhanced Coal Bed Methane (ECBM) recovery via CO₂ sequestration. Earth Sci. Rev. 179, 392–410. https://doi.org/10.1016/j.earscirev.2018.02.018.
- Nie, B., Sun, S.J., et al., 2023. Thermal recovery of coalbed methane: Modeling of heat and mass transfer in wellbores. Energy 263, 125899. https://doi.org/ 10.1016/j.energy.2022.125899.
- Pan, Z.J., Ye, J.P., Zhou, F.B., et al., 2020. CO₂ storage in coal to enhance coalbed methane recovery: A review of field experiments in China. Coal Geology of China 224–246.
- Ren, T., Wang, F.T., 2015. Gas reservoir simulation for enhanced gas recovery with nitrogen injection in low permeability coal seams. Int. J. Oil Gas Coal Technol. 10 (3), 272–292. https://doi.org/10.1504/IJOGCT.2015.071514.
- Rutqvist, J., Wu, Y., Tsang, C., et al., 2002. A modeling approach for analysis of coupled multiphase fluid flow, heat transfer, and deformation in fractured porous rock. Int. J. Rock. Mech. Min. 39 (4), 429–442. https://doi.org/10.1016/ S1365-1609(02)00022-9.
- Sayyafzadeh, M., Keshavarz, A., Alias, A.R.M.A., et al., 2015. Investigation of varying-composition gas injection for coalbed methane recovery enhancement: A simulation-based study. J. Nat. Gas Sci. Eng. 27, 1205—1212. https://doi.org/10.1016/j.jngse.2015.09.071.
- Shen, W.J., Ma, T.R., Li, X.Z., et al., 2022. Fully coupled modeling of two-phase fluid flow and geomechanics in ultra-deep natural gas reservoirs. Phys. Fluids 34 (4). https://doi.org/10.1063/5.0084975.
- Shukla, R., Ranjith, P., Haque, A., et al., 2010. A review of studies on CO₂ sequestration and caprock integrity. Fuel 89 (10), 2651–2664. https://doi.org/10.1016/ifuel_2010_05_012
- Sun, F.R., Liu, D.M., Cai, Y.D., et al., 2023. Surface jump mechanism of gas molecules in strong adsorption field of coalbed methane reservoirs. Appl. Energy 349, 121605. https://doi.org/10.1016/j.apenergy.2023.121605.
- Sun, X.F., Zhang, Y.Y., Li, K., et al., 2016. A new mathematical simulation model for gas injection enhanced coalbed methane recovery. Fuel 183, 478–488. https:// doi.org/10.1016/j.fuel.2016.06.082.
- Sun, Y.F., Zhao, Y.X., Yuan, L., et al., 2018. CO₂-ECBM in coal nanostructure: Modelling and simulation. J. Nat. Gas Sci. Eng. 54, 202–215. https://doi.org/10.1016/j.jngse.2018.04.007.
- Tupsakhare, S., Castaldi, M., 2019. Efficiency enhancements in methane recovery from natural gas hydrates using injection of CO₂/N₂ gas mixture simulating insitu combustion. Appl. Energy 236, 825–836. https://doi.org/10.1016/j.apenergy.2018.12.023.
- Vishal, V., Singh, N., Ranjith, G., et al., 2015. Influence of sorption time in CO₂-ECBM process in Indian coals using coupled numerical simulation. Fuel 139, 51–58. https://doi.org/10.1016/j.fuel.2014.08.009.

- Vishal, V., Mahanta, B., Pradhan, S., et al., 2018. Simulation of CO₂ enhanced coalbed methane recovery in Jharia coalfields, India. Energy 159, 1185–1194. https://doi.org/10.1016/j.energy.2018.06.104.
- Wang, L.C., Wang, Z.F., Li, K.Z., et al., 2015. Comparison of enhanced coalbed methane recovery by pure N₂ and CO₂ injection: Experimental observations and numerical simulation. J. Nat. Gas Sci. Eng. 23, 363–372. https://doi.org/10.1016/j.ingse.2015.02.002.
- Wei, M.G., Liu, C., Liu, Y.K., et al., 2022. Long-term effect of desorption-induced matrix shrinkage on the evolution of coal permeability during coalbed methane production. J. Petrol. Sci. Eng. 208, 109378. https://doi.org/10.1016/ i.petrol.2021.109378.
- Wu, Y., Liu, J.S., Chen, Z.W., et al., 2011. A dual poroelastic model for CO₂-enhanced coalbed methane recovery. Int. J. Coal Geol. 86 (2–3), 177–189. https://doi.org/10.1016/j.coal.2011.01.004.
- Xu, L.J., Fan, C.J., Luo, M.K., et al., 2023. Elimination mechanism of coal and gas outburst based on geo-dynamic system with stress—damage—seepage interactions. Int. J. Coal. Sci. Techn. 10 (1), 74. https://doi.org/10.1007/s40789-023-00651-z.
- Yang, L., Fan, C.J., Wen, H.O., et al., 2023. An improved gas—liquid—solid coupling model with plastic failure for hydraulic flushing in gassy coal seam and application in borehole arrangement. Phys. Fluids 35 (3). https://doi.org/10.1063/ 5.0144786

- Zarrouk, S., Moore, A., 2009. Preliminary reservoir model of enhanced coalbed methane (ECBM) in a subbituminous coal seam, Huntly Coalfield, New Zealand. Int. J. Coal Geol. 77 (1–2), 153–161. https://doi.org/10.1016/j.coal.2008.08.007.
- Zhang, C.L., Wang, E.Y., Li, B.B., et al., 2023. Laboratory experiments of CO2-enhanced coalbed methane recovery considering CO2 sequestration in a coal seam. Energy 262, 125473. https://doi.org/10.1016/j.energy.2022.125473.
- Zhang, Q., Zhu, H.Q., Kang, R.X., et al., 2023. Insights into influence of CH₄ on CO₂/N₂ injection into bituminous coal matrix with biaxial compression strain in molecular terms. J. Nat. Gas Sci. Eng. 117, 205077. https://doi.org/10.1016/i.jgsce.2023.205077.
- Zhao, W., Cheng, Y.P., Pan, Z.J., et al., 2019. Gas diffusion in coal particles: A review of mathematical models and their applications. Fuel 252, 77–100. https://doi.org/ 10.1016/j.fuel.2019.04.065.
- Zhou, F.D., Hussain, F., Cinar, Y., 2013. Injecting pure N₂ and CO₂ to coal for enhanced coalbed methane: Experimental observations and numerical simulation. Int. J. Coal Geol. 116, 53–62. https://doi.org/10.1016/j.coal.2013.06.004.
- Zhou, L.J., Zhou, X.H., Fan, C.J., et al., 2023. Modelling of flue gas injection promoted coal seam gas extraction incorporating heat-fluid-solid interactions. Energy 268, 126664. https://doi.org/10.1016/j.energy.2023.126664.
- Zhou, L.J., Zhou, X.H., Fan, C.J., et al., 2022. Coal permeability evolution triggered by variable injection parameters during gas mixture enhanced methane recovery. Energy 252, 124065. https://doi.org/10.1016/j.energy.2022.124065.